Influence of foam on the stability characteristics of immiscible flow in porous media

van der Meer, Jakolien; Farajzadeh, Rouhi; Jansen, Jan Dirk

DOI
10.2118/182662-MS

Publication date
2017

Document Version
Final published version

Published in
SPE Reservoir Simulation Conference

Society of Petroleum Engineers

SPE-182662-MS

Influence of Foam on the Stability Characteristics of Immiscible Flow in Porous Media

J. M. van der Meer, Delft University of Technology; R. Farajzadeh, Delft University of Technology, Shell Global Solutions International; J. D. Jansen, Delft University of Technology

This paper was prepared for presentation at the SPE Reservoir Simulation Conference held in Montgomery, TX, USA, 20–22 February 2017.

Abstract

Accurate field-scale simulations of foam enhanced oil recovery are challenging, due to the sharp transition between gas and foam. Hence, unpredictable numerical and physical behavior is often observed, casting doubt on the validity of the simulation results. In this paper a thorough stability analysis of the foam model is presented, to validate the simulation results and lay a foundation for a tailor-made solver, which can both handle large-scale reservoir simulations and accurately resolve front instabilities. We study the effect of a strongly non-monotonous total mobility function arising from foam models on the stability characteristics of the flow. To this end, we generalize the linear stability analysis of Riaz and Tchelepi (2004–2007) to nearly discontinuous relative permeability functions, and compare the results with those of highly accurate numerical simulations. In addition, we present a qualitative analysis for the effect of different reservoir and fluid properties on the foam fingering behavior. In particular, we consider the effect of heterogeneity of the reservoir, injection rates, and foam quality. Relative permeability functions play an important role in the onset of fingering behavior of the injected fluid (Riaz and Tchelepi, 2006a). Hence, we can deduce that stability properties are highly dependent on the nonlinearity of the foam transition. The foam-water interface is governed by a very small total mobility ratio, implying a stable front. The transition between gas and foam, however, exhibits a huge total mobility ratio, leading to instabilities in the form of viscous fingering. This implies that there is an unstable pattern behind the front. An indication of this behavior was shown in (Farajzadeh et al., 2016) for a similar foam model, but the authors did not provide a satisfying explanation for the cause of these instabilities. Here we closely study the influence of the foam on instabilities at and behind the front, and are able to predict the flow stability for different foam qualities. We deduce that instabilities are indeed able to grow behind the front, but are later absorbed by the expanding wave. The stability analysis, validated by numerical simulations, provides valuable insights about the important scales and wavelengths of the foam model. In this way we remove any ambiguity regarding the effect of grid resolution on the convergence of the solutions. This makes it possible to design a suitable computational solver that captures all the appropriate scales, while retaining computational efficiency.

Introduction

Foam enhanced oil recovery (EOR) is applied to increase oil production by reducing disadvantageous effects like channeling, viscous fingering, and gravity override. When gas is injected in a porous medium containing a surfactants solution, a foam front forms. The foam captures the gas in bubbles and reduces its mobility. The effectiveness of the process depends on the stability of the created foam controlled by the magnitude of the capillary pressure. It has been observed that foam experiences a significant coalescence when the capillary pressure approaches the so-called limiting capillary pressure, P_c^* Khatib et al., 1988; Farajzadeh e t al., 2015). In other words, when the water saturation drops below a critical value called the limiting water saturation, S_w^*, foam becomes too dry and collapses. The mobility of the gas, which is the ratio of the relative gas permeability and the gas viscosity, therefore contains a sharp transition around the limiting water saturation.

To reduce the operational risks associated with the injectivity decline (because of generation of very strong foams) and the material compatibility as well as the well integrity, it is suggested to inject the gas and the surfactant solution in alternating mode, i.e., a slug (fraction of the pore volume) of surfactant followed by a slug of gas. Upon mixing of the gas and the surfactant solution in the pores, foam lamellae will form in-situ. Behind the foam front, gas reduces the water saturation to saturations close to the limiting water saturation and therefore with gradual or abrupt collapse of foam, the gas mobility increases from the foam front towards the injection well. The instabilities that might occur within this bank (between the front and the injection point) has been the subject of study by Farajzadeh et al. (2016), who suggested that the fingering has physical origin and is not due to numerical artifacts discussed in the paper.

This phenomenon, the extent of which depends mainly on the properties of the foam behind the front, may not be visible in simulations with poor grid resolutions.

Because of this aspect of foam, accurate field-scale simulations are challenging. Hence, unpredictable numerical and physical be havior is often observed, casting doubt on the validity of the simulation results (Ashoori et al., 2011, 2012; Namdar Zanganeh et al., 2014; Boeije and Rossen, 2015; Farajzadeh et al., 2016). In this paper a thorough stability analysis of a (implicit texture, local equilib rium) foam model is presented, to validate the simulation results and lay a foundation for a tailor-made solver, which can both handle large-scale reservoir simulations and accurately resolve front instabilities. We study the effect of a strongly non-monotonous total mobility function arising from foam models on the stability characteristics of the flow. To this end, we generalize the linear stability analysis of (Yortsos and Hickernell, 1989; Riaz and Tchelepi, 2004; Riaz et al., 2005; Riaz and Tchelepi, 2006a, 2007; Meulenbroek et al., 2013) to nearly discontinuous relative permeability functions, and compare the results with those of highly accurate numerical simulations.

In this earlier work on the stability of immiscible two-phase flow in porous media, a linear stability analysis was performed for the quasi-linearized model. This was done in a transformed coordinate frame that moves along with the front. By using a perturbation theory that exploits a normal mode decomposition strategy, it was shown that the onset of the instabilities of the displacing fluid is governed by the total mobility ratio across the shock (as opposed to the mobility ratio over the entire transition region). The shape of the relative permeability curves plays an important role at this stage (Riaz and Tchelepi, 2006a).

We therefore propose to apply the perturbation theory on the foam model, to investigate the effect of the abrupt changes in the gas relative permeability on the stability of the foam front. We are especially interested in the effect of this particular relative permeability function on the stability characteristics of the model. The function form differs from the ones described by Riaz and Tchelepi (2006a), because it allows for discontinuities and the corresponding total mobility function is non-monotonic, which can have an unfavorable shock-mobility ratio.

The foam-water interface has usually a very small total mobility ratio, leading to a stable front. The subsequent transition front, where foam turns into gas, exhibits a large total mobility ratio. This implies

that there is an unstable pattern behind the front, which could only be detected by highly-accurate numerical simulations. An indication of this behavior was shown in Farajzadeh et al. (2016) for a two-phase incompressible immiscible foam model. The question is to which extent the strong non-linearities in the foam model can be described by a linear stability analysis. To answer this, we compare the linear stability results with accurate numerical simulations, where we approximate several properties, like interfacial length, wave number and maximum growth number. To solve the system of saturation and pressure equations we apply a sequential implicit finite volume method. To minimize numerical diffusion around the front we use a second-order monotonic upstream-centered scheme for conservation laws (MUSCL) for the hyperbolic flux functions and a central scheme to compute the pressure values. Both equations contain a strongly nonlinear mobility function, and therefore the system is considered stiff. Hence, the time step of the numerical scheme is very restricted, and the numerical scheme exhibits stability issues. To improve the stability of the numerical scheme a Taylor-Galerkin method is applied to the entire system. The nonlinearity is accounted for by introducing auxiliary variables (Ambrosi and Quartapelle, 1998). Using this scheme we are able to resolve the very fast wave speeds that emerge from the nonlinearity of the model.

The structure of the paper is as follows: first we introduce the two-phase foam model, and discuss its characteristics in Section 2. For this model, a linear stability analysis is performed in Section 3. The results from this analysis, are then compared to numerical simulations discussed in Section 4. Finally, we discuss the outcomes of both analyses in Section 6.

Foam model

We use the non-dimensional model described by Riaz and Tchelepi (2007), for the injection of an incompressible gas into a porous rock initially filled with water, which is given by

$$\partial_t S = -\nabla\left(\frac{Mk_{rg}}{\lambda}\mathbf{u} + G\frac{k_{rg}k_{rw}}{\lambda}\nabla z + \frac{k_{rg}k_{rw}}{N_{ca}\lambda}\frac{dP_c}{dS_w}\nabla S\right) = -\nabla\cdot(k_{rw}\nabla\bar{P}), \tag{1}$$

$$\nabla\mathbf{u} = 0, \tag{2}$$

$$\mathbf{u} = -\lambda\nabla\bar{P} + Gk_{rg}\nabla z + \frac{1}{N_{ca}}k_{rg}\frac{dPc}{dS_w}\nabla S, \tag{3}$$

where $S = (S_g - S_{gr})/(1 - S_{wc} - S_{gr})$ is the normalized gas saturation, $\nabla\bar{P} = \nabla P_w + (\rho w g k/\mu_w U)\nabla z$ the scaled pressure, u the total Darcy velocity, and $\lambda = Mk_{rg} + k_{rw}$ the dimensionless mobility function. The variables M, G and N_{ca} denote the dimensionless end-point mobility ratio, gravity number and capillary number respectively, which are given by

$$M = \frac{\mu_w}{\mu_g}\frac{k_{rge}}{k_{rwe}}, \tag{4}$$

$$G = \frac{k\Delta\rho g}{\mu_g U}, \tag{5}$$

$$N_{ca} = = \frac{\mu_g UW}{\gamma_{gw}\sqrt{\phi k}}, \tag{6}$$

where W is a characteristic length scale of the model where viscous and capillary terms are of comparable magnitude (Yortsos and Hickernell, 1989), and U is a characteristic velocity, which is set equal to the gas injection rate. The other parameters are explained in Appendix A. We consider the one dimensional version of this equations with $\mathbf{u} = 1$, given by

$$\partial_t S + \partial_x\left(f(S) + \frac{k_{rg}k_{rw}}{N_{ca}\lambda}\frac{dP_c}{dS_w}\frac{dS}{dx}\right) = 0, \tag{7}$$

If capillary pressure is neglected (Ca→ ∞) this equation is the Buckley-Leverett equation with a non-convex flux

$$f = \frac{Mk_{rg}}{\lambda}\left(1 + G\frac{k_{rw}}{M}\right), \tag{8}$$

for which we can derive the characteristic solution. The characteristics of this solution depend on the form of the normalized relative permeability functions k_{rw} and k_{rg}, which are given by

$$k_{rg} = \frac{S^{n_g}}{f_{mr}}, \quad f_{mr} = 1 + R \cdot F_w, \tag{9}$$

$$k_{rw} = (1 - S)^{n_w}, \tag{10}$$

where f_{mr} is the mobility reduction factor due to foam generation, R is a constant that accounts for the maximum flow resistance of the foam. The function F_w describes the dependency of the foam strength to water saturation, and is given by

$$F_w = 0.5 + \frac{\arctan(\kappa(S_w - S_w^*))}{\pi}, \tag{11}$$

where S_w* represents the limiting water saturation and κ is a positive parameter that controls the width of the gas-foam transition. For κ = ∞ the gas-foam transition is instant (Fig. 1a), and no foam exists below S_w*. For smaller values of κ, the mobility reduction of foam (i.e. foam strength) increases as the water saturation increases in the transition zone (Fig. 1b) In other words, foam collapse occurs over a range of water saturation whose width is determined by κ. The corresponding flux functions and derivatives are shown in Fig. 2.

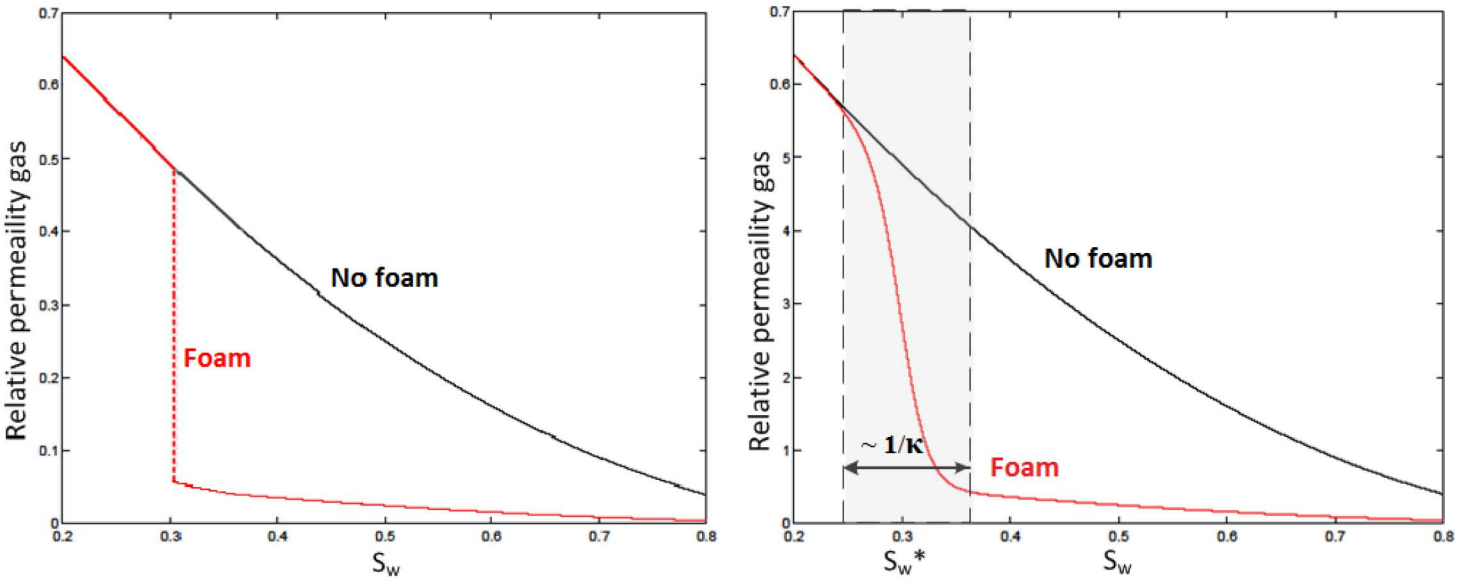

(a) κ = ∞ (b) κ = 40

Figure 1—Relative permeability function for the model with (f_{mr} > 1) and without foam (f_{mr} = 1). The sudden drop in relative gas permeability due to foam is shown for different transition rates κ, for S_w* = 0.3, R = 10, M = 1 and G = 0 (Van der Meer et al., 2014).

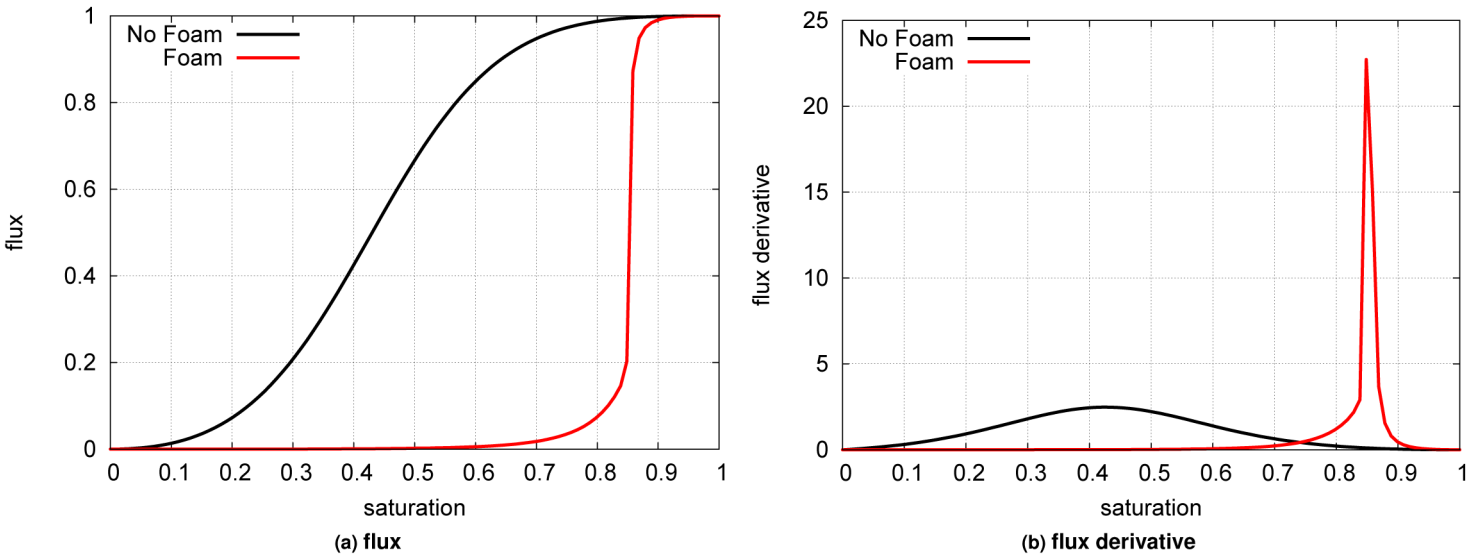

(a) flux (b) flux derivative

Figure 2—Flux function and flux derivative for the model with and without foam, for S_w^* = 0.15, κ = 1000, R = 1000, M = 1 and G = 0 (Van der Meer et al., 2014).

The characteristic solution of the Buckley-Leverett equation with the given relative permeability functions consists of a rarefaction and a right moving shock wave as shown in Fig. 3. The shock-speed v_s can be determined from

$$v_s = \left.\frac{df(S)}{dS}\right|_{S_s} = \frac{f(S_s) - f(S_i)}{S_s - S_i}, \tag{12}$$

where S_s is the shock saturation, and $S_i = 0$ is the initial gas saturation in the porous medium. For saturation values larger than S_s the solution consists of a rarefaction wave, for which $x/t = f'(S(x,t))$ (LeVeque, 1992).

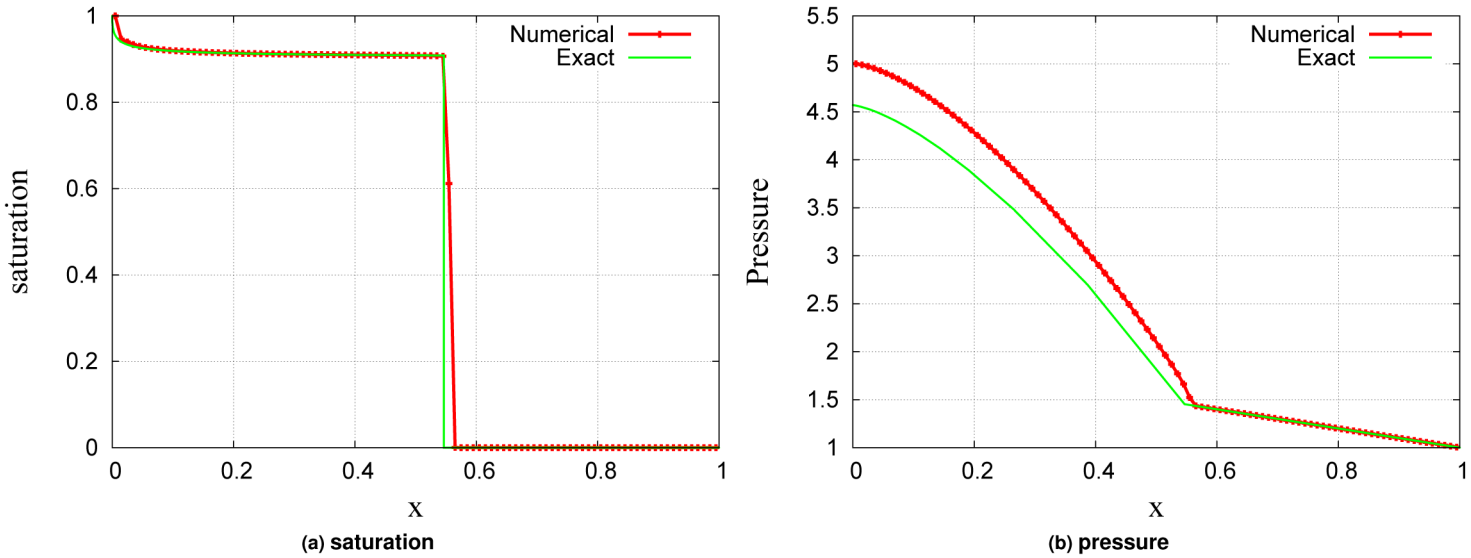

(a) saturation (b) pressure

Figure 3—Solution of the Buckley-Leverett equation at t = 0.05, for S_w^* = 0.1, κ = 1000, R = 10000, M = 1 and G = 0.

Linear stability analysis

To analyze the influence of foam on the stability characteristics of the fluid displacement, we perform a linear stability analysis on Eq. 1 and 2, where we start off with the full system including capillarity. To do so, we linearize the equations around a base state, that is given by the characteristic solution of the one-

dimensional version of the saturation equation, Eq. 7. For this equation a self-similar solution exists as a function of $\xi = x - v_s t$, in the neighborhood of the Buckley-Leverett shock where $\xi = 0$, which does not change in time (Yortsos and Hickernell, 1989). This solution can be used as the base state (S_0,P_0) for the stability analysis, which is given by (Riaz and Tchelepi, 2007)

$$\frac{dS_0}{d\xi} = \frac{\lambda \mathrm{Ca}}{k_{rw}k_{rg}P_c'}\left(v_s S_0 - f(S_0)\right), \tag{13}$$

$$\frac{dP_0}{d\xi} = \frac{1}{\lambda}\left(Gk_{rg} + \frac{k_{rg}}{Ca}P_c'S_0' - 1\right). \tag{14}$$

In the absence of capillarity ($\mathrm{Ca} \to \infty$) the base state satisfies (Riaz and Tchelepi, 2007)

$$\frac{S_0}{d\xi} = \delta(\xi), \tag{15}$$

$$\frac{dP_0}{d\xi} = \frac{Gk_{rg} - 1}{\lambda}, \tag{16}$$

We can expand the full solution in terms of the base state and a perturbation function. The last is written as a set of streamwise eigenfunctions $\hat{s}$ and $\hat{p}$ times a normal mode series, such that

$$(S,P)(\xi,y,t) = (S_0,P_0)(\xi) + (\hat{s},\hat{p})(\xi)\mathrm{e}^{iny+\sigma t}, \tag{17}$$

where n denotes the wavenumber of the perturbation and σ the wave growth rate. Substituting this eigenmode expansion into Eq. 1 and 2, and solving the resulting eigenvalue problem (Riaz and Tchelepi, 2004, 2007), leads to an expression for the disturbance velocity:

$$\frac{\sigma}{n} = \frac{f_{g_1} - f_{g_0}}{S_1 - S_0}\frac{\lambda_1(1 - Gk_{rg_0}) - \lambda_0(1 - Gk_{rg_1})}{\lambda_1 - \lambda_0}, \tag{18}$$

where the subscripts 0 and 1 denote the front and back edge of the shock respectively. The derivation of these equations can be found in Appendi x B. If there is no gravity influence ($G = 0$), i.e. we consider a horizontally located reservoir, this becomes

$$\frac{\sigma}{n} = \frac{f_{g_1} - f_{g_0}}{S_1 - S_0} = v_s\Lambda, \tag{19}$$

$$\Lambda = \frac{M_s - 1}{M_s + 1}, \tag{20}$$

where $M_s = \lambda_1/\lambda_0$, the mobility ratio across the shock, and Λ is the disturbance number. Hence we see, that this number is positive if $M_s > 1$, which means the flow is unstable at the shock. Vice versa, a mobility ratio smaller than one leads to a stable displacement accordingly. If gravity is included it has been shown by (Riaz and Tchelepi, 2007), that

$$G(k_{rg_1} - M_s k_{rg_0}) < 1 - M_s \tag{21}$$

to obtain stable displacement. If capillarity is included, apart from the shock mobility ratio the fractional flow profiles have an influence on the stability of the flow. In the limit of small wave numbers the disturbance velocity can therefore be extended to a higher-order formulation (Yortsos and Hickernell, 1989), given by

$$\sigma = \Gamma_1 n + \Gamma_2 n^2 + \Gamma_3 \ln\left(n(s_1 - s_0)\right)n^2, \tag{22}$$

where $\Gamma 1$ is given by Eq. 18 and $\Gamma 2$ and $\Gamma 3$ are determined by the derivative of the total mobility and the fractional flow profiles.

Stability results

The above analysis for the model without capillarity and gravity allows us to investigate the influence of foam on the viscous instability at the front. Based on the results of (Farajzadeh et al., 2016), different scenarios are addressed: a weak foam (low mobility reduction factor, case 1), three cases of a strong foam (high mobility reduction factor, case 2 to 4) with different transition lengths from foam to gas, and a fifth case with the effect of gravity included (see Fig. 4 and Fig. 5).

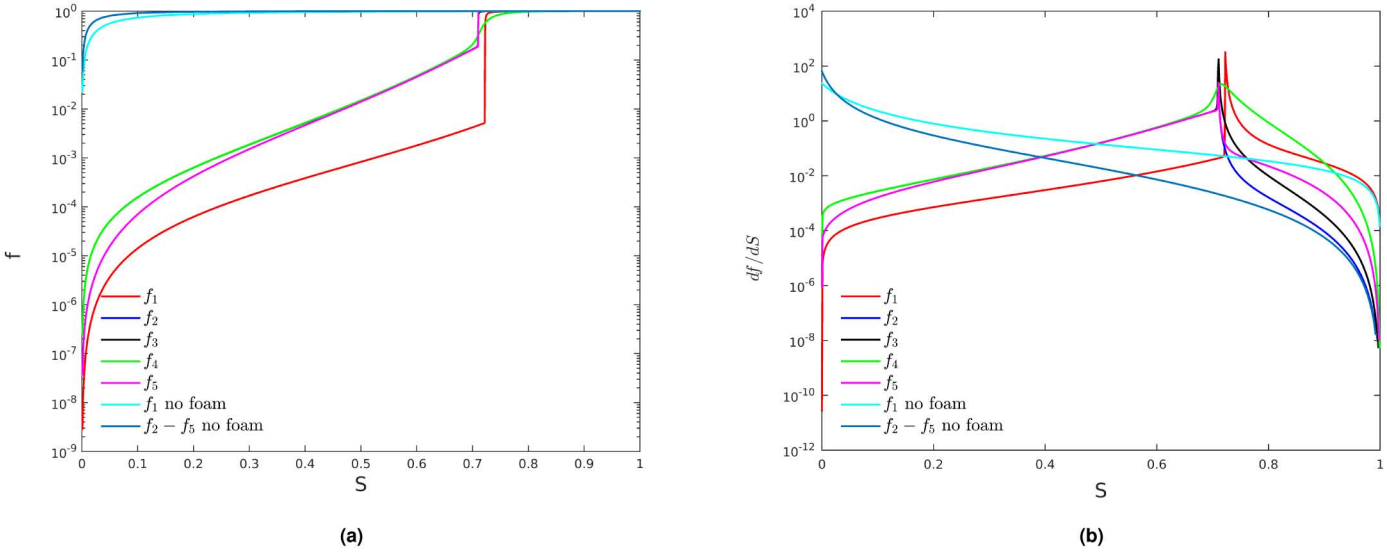

Figure 4—(a) Flux functions and (b) flux derivative/wave speed for the five test cases of (Farajzadeh et al., 2016) and two reference cases without foam.

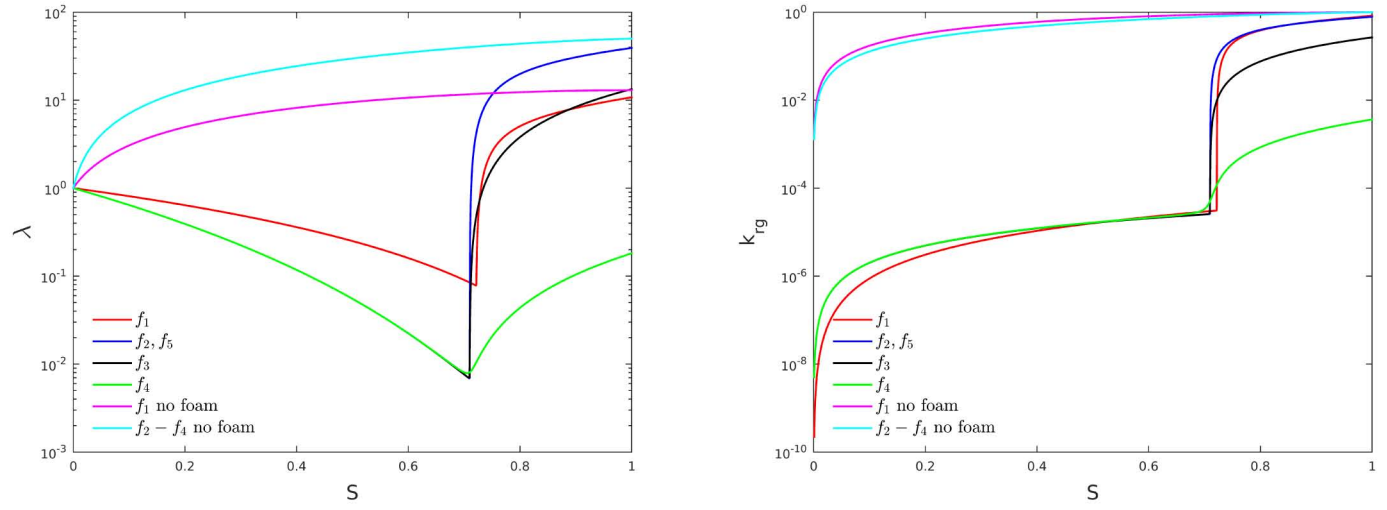

Figure 5—(a) Total mobility and (b) relative permeability gas versus the gas saturation for the five test cases of Farajzadeh et al. (2016).

Since we only looked at the linearized model without capillarity, there is no damping at large wave numbers (Riaz and Tchelepi, 2007), and hence the wave growth is a linear increasing function of the wave number. Moreover, the base state of the model without capillarity contains a shock wave at $S_0 = S_s = \max_S \frac{f_g(S)-f_g(S_R)}{S-S_R}$, that marks the interface between gas and water. The shock wave is followed by a rarefaction wave, where water and gas co-exist. As shown in Fig. 6a the shock saturation of water (gas) is almost everywhere smaller (larger) than the limiting water (gas) saturation, i.e. the saturation that marks the transition from gas

to foam. Therefore, only due to a numerically and/or physically dispersed shock (denoted by red dashed lines), or a very wide transition range of foam (denoted by blue dashed lines), foam can exist in this model. The second plot (Fig. 6b) shows that the shock speed increases with the limiting water saturation, because strong foam slows down the front significantly. It follows from Eq. 19 that the viscous instability increases linearly with the shock speed. Thus a strong foam has less instabilities than a weak foam, according to this analysis. This corresponds to the results obtained by Farajzadeh et al. (2016).

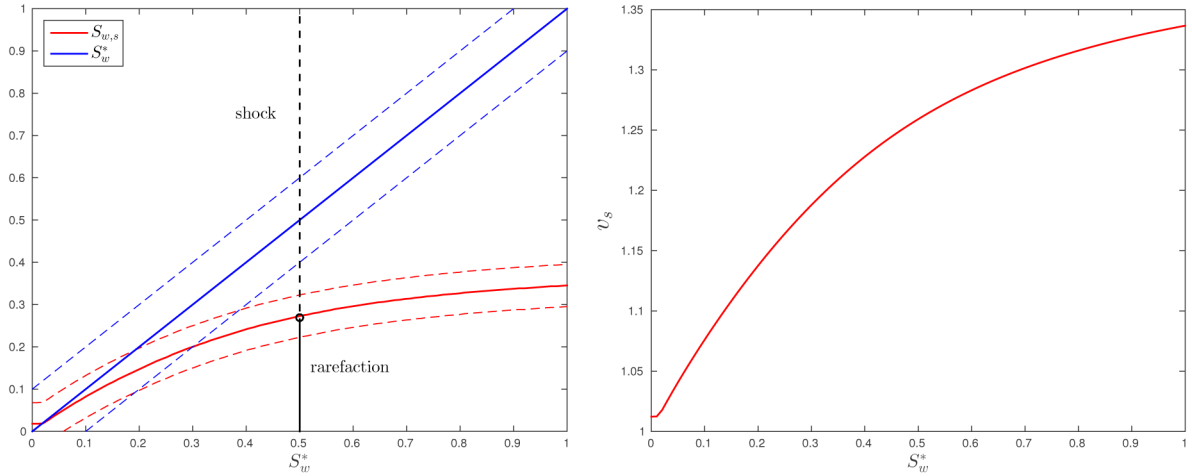

Figure 6—(a) Shock saturation versus the limiting water saturation, for κ = 1000, *R* = 1000, and *G* = 0. (b) Shock speed versus the limiting water saturation, for κ = 1000, *R* = 1000, and *G* = 0. The red dashed lines indicate the diffusion around the shock, because of capillarity and/or numerical diffusion. The blue dashed lines indicate the transition width of the foam, which is governed by the inverse of κ.

We can also examine the influence of the mobility ratio on the growth rate of the various test cases described in Farajzadeh et al. (2016), as depicted in Fig. 7a. As the mobility ratio increases the growth rate also increases. For small mobility ratio the growth rate increases very fast for the fifth test case f_5, after which it scales with approximately $M^{1/2}$, which is similar to what Riaz and Tchelepi (2004) observed for their test cases without foam. The first three cases including foam (denoted by f_1, f_2, f_3), show an overall increase of $M^{1/2}$ and the fourth test case f_4 has a more or less constant growth number which is always smaller than zero. This implies that the fourth test case is always stable, whereas the first test case is always unstable ($\sigma/n > 0$). The other three test cases are unstable at the shock front for larger mobility ratios only, according to this analysis. Also, if we have a look at the mobility ratio across the shock depicted in Fig. 7**b**, we see the same pattern. For the fourth test case the shock ratio $M_s < 1$ for all M, which is according to our expectations and implies a stable displacement for all values of M. For the first test case $Ms > 1$ for all M, implying an unfavorable displacement, with instabilities. The other three test cases have an unfavorable mobility ratios for values of $M > 10$. Moreover, for large viscosity ratios we observe a oscillatory pattern due to total mobility values, that are very sensitive to small changes in the parameters (see Fig. 5a).

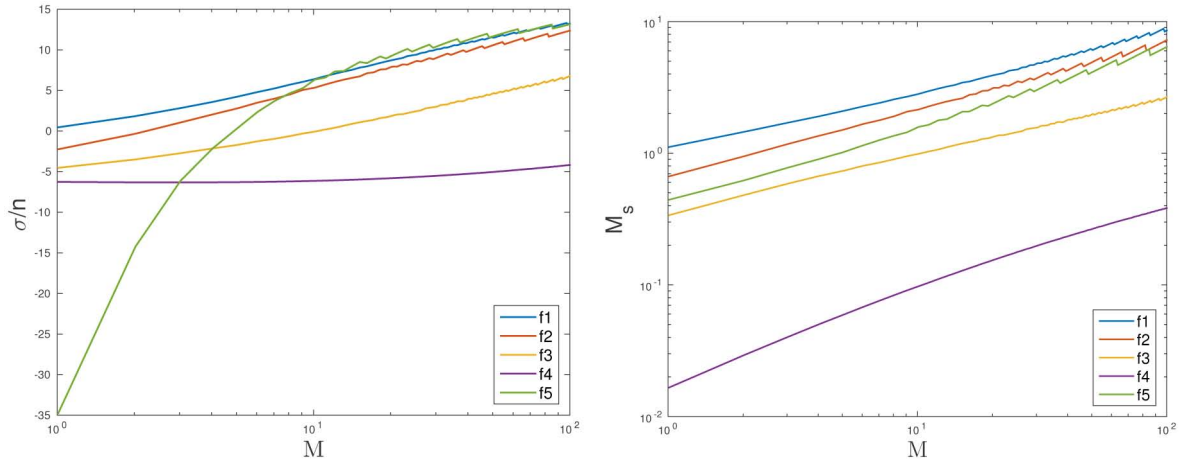

Figure 7—(a) Growth rate versus the mobility ratio M (b) Total mobility ratio across the shock versus M, for the five test cases of Farajzadeh et al. (2016)

Since the foam models are characterized by the parameters R, κ and θ, we studied the influence of these parameters on the dimensionless growth number Λ. Figure 8 shows the contour lines of the growth number in the κ - R plane, for the remaining parameter sets of test case one and two of Farajzadeh et al. (2016). The stable region for the parameter set of the first parameter set defined in Table 1 is much larger than for the parameter set of test case 2 to 4. This is not an effect of the mobility ratio, which is larger for the second parameter set (M_2 = 235 vs M_1 = 61), and hence has to be due to a difference in the form of the relative permeability functions because of different values of n_w and n_g (see (Riaz and Tchelepi, 2006a) for a thorough description of the influence of those parameters on the dimensionless growth number). We also observe that the stability contour lines, which are set by the dimensionless growth number, are all straight with a positive angle. This means that an increasing mobility reduction factor (R) has a stabilizing effect, while an increasing non-linearity (κ) has a destabilizing effect. Hence, a strong foam (higher R with a small transition width κ) is usually stable, while a weak foam (lower R) can become unstable quickly for relatively low values of κ. Test case 1 and 2, are examples of a weak and a strong foam that are unstable, while test case 3, 4 and 5 are stable according to this analysis. Finally we see, that between the region of instability and stability there is a zone, which can be both stable and unstable. This is due to a strong sensitivity of the shock mobility to the foam parameters κ and R, especially for increasing values of R. Overall, we can deduce that the contour lines of the dimensionless growth number are linear, and hence we can write

$$\frac{\partial \Lambda}{\partial R} + a(\Lambda)\frac{\partial \Lambda}{\partial \kappa} = 0, \quad a(\Lambda) = \frac{d\kappa}{dR}, \tag{23}$$

Table 1—Simulation parameters for the four test case of Farajzadeh et al. (2016).

Parameter	Case 1	Case 2	Case 3	Case 4	Explanation
R	$1.8 * 10^4$	$2.5 * 10^4$	$2.5 * 10^4$	$2.5 * 10^4$	maximum resistance foam to flow
S_w*	0.268	0.29	0.29	0.29	critical water saturation
κ	10^5	10^5	10^4	0^2	steepness parameter foam transition
k_{rge}	0.94	0.94	0.94	0.94	endpoint relative permeability gas
k_{rwe}	0.2	0.2	0.2	0.2	endpoint relative permeability water
L_x	0.8	0.8	0.8	0.8	x-correlation length absolute permeability
Ly	0.05	0.05	0.05	0.05	y-correlation length absolute permeability
$\mu_g\,[Pa \cdot s]$	$5 \cdot 10^{-5}$	$2 \cdot 10^{-5}$	$2 \cdot 10^{-5}$	$2 \cdot 10^{-5}$	gas viscosity

Parameter	Case 1	Case 2	Case 3	Case 4	Explanation
$\mu_w\ [Pa \cdot s]$	$0.65 \cdot 10^{-3}$	10^{-3}	10^{-3}	10^{-3}	water viscosity
n_g	1.8	1.3	1.3	1.3	power coefficient of gas
n_w	2	4.2	4.2	4.2	power coefficient of water
$\rho_g\ [kg/m^3]$	10^{-5}	10^{-5}	10^{-5}	10^{-5}	gas density
$\rho_w\ [kg/m^3]$	10^{-5}	10^{-5}	10^{-5}	10^{-5}	water density
$S_{g,r}$	0.0	0.0	0.0	0.0	residual gas saturation
$S_{w,c}$	0.0	0.0	0.0	0.0	critical water saturation
$S_{g,inj}$	1.0	1.0	1.0	1.0	injected gas saturation
$I\ [m^3/s]$	$3.5 \cdot 10^{-5}$	$3.5 \cdot 10^{-5}$	$3.5 \cdot 10^{-5}$	$3.5 \cdot 10^{-5}$	injection relative permeability gas
$K\ [mm^2]$	$5 \cdot 10^{-10}$	$5 \cdot 10^{-10}$	$5 \cdot 10^{-10}$	$5 \cdot 10^{-10}$	absolute permeability (mean value)
ϕ	0.2	0.2	0.2	0.2	porosity

where the slope $a = \frac{\Delta\kappa}{\Delta R}$ is constant along the contour lines, and can be linked to the growth of disturbances in the κ - R space. This speed is highest for low R and high κ values.

The influence of the limiting water saturation S_w*is more complicated as can be seen in Fig. 9 and Fig. 10. These figures depict the disturbance velocity, and show that the solutions are only stable for low values of the critical water saturation. This can be partly explained by Fig. 6a, which shows that the region where foam can exist for this model is limited to values of $S_w^* < 0.4$. Hence, a larger limiting water saturation, implies that there is no foam present and hence that instabilities at the front are not subdued by foam. Moreover, we observe that the region of the highest disturbance velocities is located around $S_w^* = 0.6$ for the first parameter set, and around $S_w^* = 0.9$ for the second parameter set. As can be deduced from Fig. 8 the growth number is highest for low R and high κ. So, even if there is no foam present, the choice of S_w*influences the stability of the solutions, since both the shock saturation and the shock velocity increase with an increasing limiting water saturation (see Fig. 6). The disturbance velocity scales linearly with the shock velocity and hence will increase too. The dimensionless growth number depends on the mobility ratio around the shock, which will be larger if the shock saturation increases. Hence, we see that large values of S_w*introduce a non-physical effect in the model by changing the shock saturation, although foam is absent. However, foam models that are used in practice are only applied for small limiting saturation values in combination with a non-zero transition width (Boeije and Rossen, 2013).

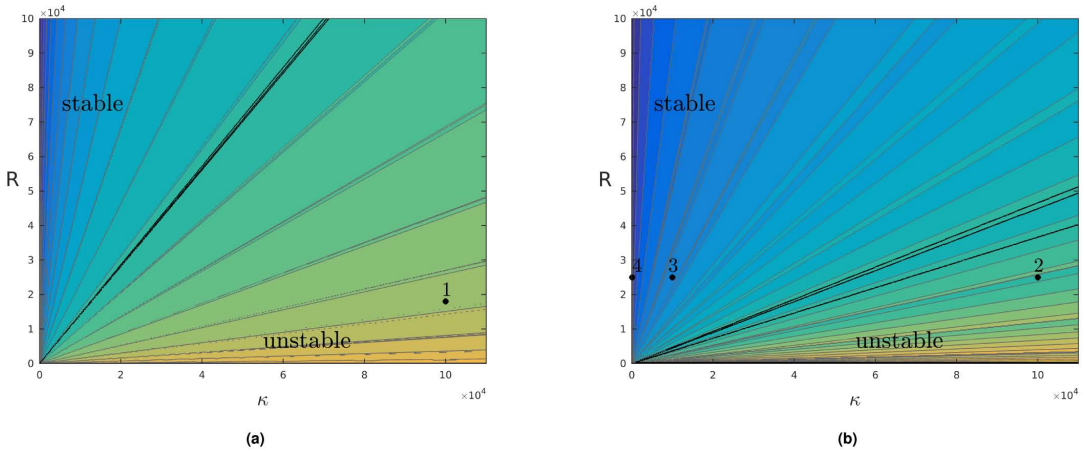

(a) (b)

Figure 8—Stability regions in the κ - R plane for the rest of the parameter set of (a) test case one, and (b) test case two of Farajzadeh et al. (2016). The stable and unstable regions are separated by the thick black lines and the different test cases are denoted by thick black dots.

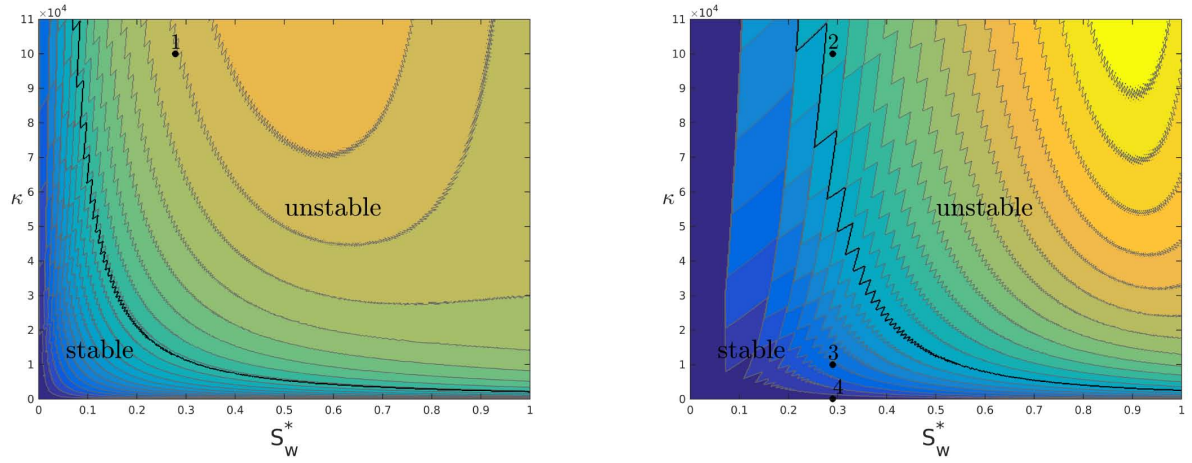

Figure 9—Stability regions in the θ - κ plane for the rest of the parameter set of (a) test case one, and (b) test case two of Farajzadeh et al. (2016). The stable and unstable regions are separated by the thick black lines and the different test cases are denoted by thick black dots.

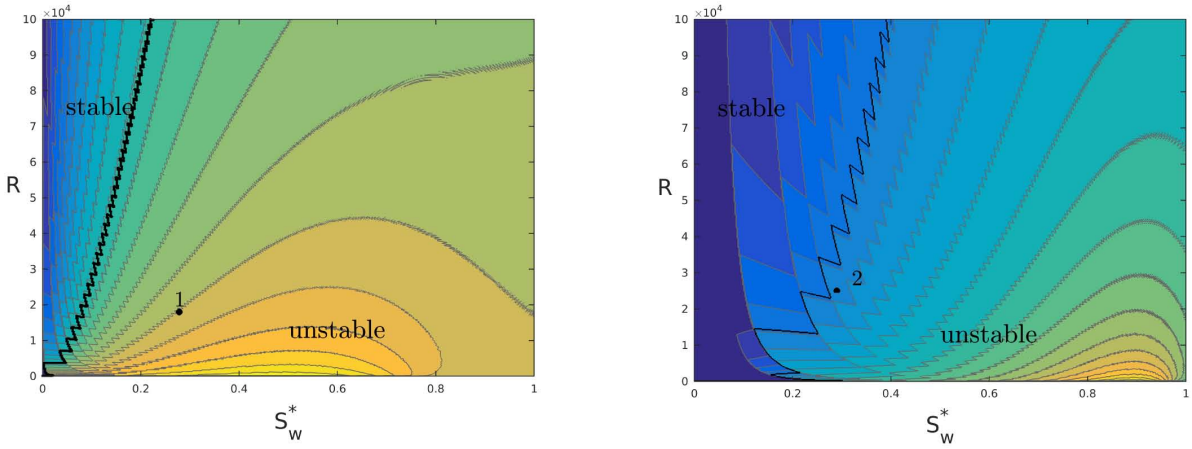

Figure 10—Stability regions in the θ - *R* plane for the rest of the parameter set of (a) test case one, and (b) test case two of Farajzadeh et al. (2016). The stable and unstable regions are separated by the thick black lines and the different test cases are denoted by thick black dots.

Numerical results

The results from the linear stability analysis can be compared with the results obtained by high resolution two-dimensional numerical simulations of foam on a rectilinear grid with a horizontal injection well. We address the same test cases as in (Farajzadeh et al., 2016). For the second case, an interesting artifact was observed in the apparent viscosity of the foam in the form of a fingering pattern behind the foam front (Fig. 11). These fingers did not significantly influence the saturation behind the front. Therefore it was not completely clear from these results whether this is a a physical effect or a numerical artifact. To analyze this effect, and validate the numerical simulations of the foam model we repeat the first four test cases of Farajzadeh et al. (2016).

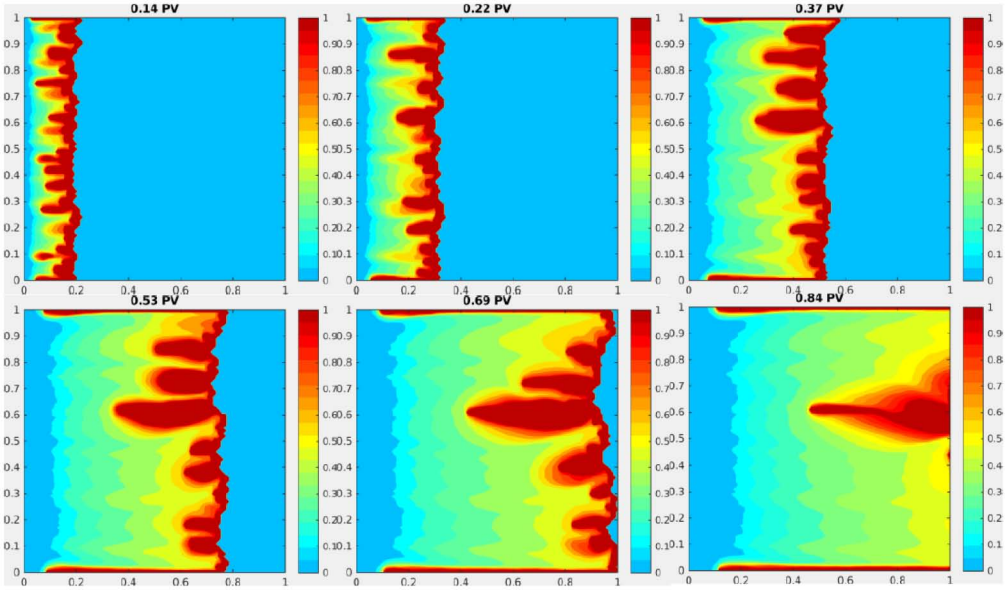

Figure 11—Instabilities in the apparent viscosity $\mu_f = \mu_g \cdot f_{mr}(S)$, (Farajzadeh et al., 2016).

Instead of solving the equations in a fully implicit way, we opt for the implicit pressure explicit saturation (IMPES) method, which is designed for this kind of hyperbolic-elliptic problems because it takes into account the different nature of the equations. Additionally, solving the saturation equation explicitly with a higher-order scheme introduces less artificial diffusion. This is important in this case, because we are interested in the detailed fingering behavior at the front and behind the front. By using operator splitting, as described in Hvistendahl Karlsen et al. (2001), we can split the saturation equation into a hyperbolic conservation law and an ordinary differential equation (ODE) for the mass flow rate. They are solved sequentially using a second-order Strang splitting scheme, which preserves the symmetry of the operator. The hyperbolic equation is solved with a second-order MUSCL scheme, which is a total variation diminishing finite volume method reconstructed from the first-order Godunov's method (Toro, 2009). The TVD property prevents instabilities to occur that are due to the numerical method. In other words a TVD scheme is monotonicity preserving if the Courant-Friedrichs-Levy (CFL) condition on the time step is satisfied (Toro, 2009). The ODE is solved by the second-order trapezoidal rule, which is A-stable and therefore suitable for stiff ODEs (Dahlquist, 1963). The size of the time step of an A-stable method does not suffer from stringent restrictions and the choice only depends on the desired accuracy. For the elliptic equation 2 we use a multigrid linear solver that combines a five-point stencil with a nine-point stencil that is rotated by 45 degrees to reduce the grid orientation effect (Wirnsberger, 2012). The five-point stencil accounts for the unrotated coefficients and is combined with a nine-point stencil that accounts for the rotated coefficients and is projected back onto the original grid. The domain is parallelized by MPI using the HYPRE library (Falgout and Meier Yang, 2002) to speed up the computations, since roughly 73% of the simulation time is spent on the pressure solver for this model (Yahya Afiff, 2014).

The foam displacement is modeled in a reservoir of size $1x1x1$ m, discretized using 300 grid blocks in the first two directions and one grid block in the z-direction (hence we have a 2D model). The porous medium of the model, has porosity $\psi = 0.2$, and a log-random permeability field with an average permeability $K = 5 \cdot 10^{-10}\text{m}^2$, a Dykstra-Parsons coefficient of 0.3 and correlation lengths $L_x = 0.5$ and $L_y = 0.01$. Initially the reservoir is filled with only water, mixed with surfactants and pure gas is injected with a fixed injection rate I, via a horizontal injector along the entire left side of the reservoir. Water and gas are then produced via a horizontal producer along the right side of the reservoir, keeping the pressure constant at 50 bar. In Table 1 the parameter values for each of the cases are specified. Note that we rounded off the power coefficients n_w and n_g, which are specified in this table, for computational efficiency reasons.

Numerical stability analysis

To compare the stability results of Section 3 with numerical simulations, we can approximate the growth rate σ numerically (Riaz and Tchelepi, 2004), by the vorticity norm

$$\bar{\omega} = \sqrt{\int_0^1 \int_0^1 \omega^2 dxdy}, \tag{24}$$

where

$$\omega = \frac{1}{\lambda_T} \frac{d\lambda_T}{dS} \nabla S \times u, \tag{25}$$

is a measure of the rotation at the finger tips. The maximum growth rate can then be approximated by:

$$\sigma_{\max} \approx \ln\left(\frac{\bar{\omega}(t)}{\bar{\omega}(t-\Delta t)}\right)/\Delta t. \tag{26}$$

The dominant mode can be measured numerically as a function of time, using the energy spectrum of the solutions, so that

$$n_{\max} \approx \frac{\int_0^K kE(k,t)dk}{\int_0^K E(k,t)dk}, \tag{27}$$

where E is the energy spectrum, computed by (Riaz and Tchelepi, 2006b):

$$E(k,t) = \left(\int_0^1 \left[\int_0^1 \omega(x,y,t)dx\right] e^{-ikt} dy\right)^2. \tag{28}$$

The disturbance number Λnum, which is a measure of perturbation growth with respect to the front speed, can then be approximated by

$$\Lambda_{\text{num}} = \frac{\sigma_{\max}}{n_{\max}}. \tag{29}$$

Likewise the interfacial length Γ, which is a measure for the amount of fingering or instability going on, can be approximated numerically (Riaz and Tchelepi, 2004) by

$$\Gamma \approx \int_0^1 \int_0^1 \sqrt{\left(\frac{\partial S}{\partial x}\right)^2 + \left(\frac{\partial S}{\partial y}\right)^2} dxdy \tag{30}$$

In the next sections these quantities were approximated and discussed for the first four test cases of Farajzadeh et al. (2016). Also, the resulting saturation and vorticity profiles for those and two reference cases are discussed below.

Test case 1

Test case 1 describes a foam displacement process with a relatively low resistance of foam to flow (R), and a low critical water saturation (S_w*), which means that the apparent viscosity of foam μ_f is still much higher than the water viscosity μ_w. Hence the flow is characterized by instabilities, like viscous fingering as shown in Fig. 12. This is reflected in the approximated interfacial length, growth rate and vorticity norm of the simulation. In Fig. 13 we see that the interfacial length shows three stages, starting off very fast for small times, and then a very slow descent, while finally getting almost constant. Compared to the case without foam, the initial growth is larger, but while the no foam case slows down eventually due to merging of small fingers into big ones (Yortsos and Hickernell, 1989; Riaz and Tchelepi, 2004), the interfacial length for this weak foam case keeps increasing over the observed period of time. It could be the case, that a larger reservoir is needed for the interfacial length to decrease. Moreover, the approximated interfacial length

summarizes over the squared partial derivatives in each grid block. Since, the foam model contains a peak in the derivative around the critical saturation, this approximation overestimates the total interfacial length at the front. This measure is therefore more suited to compare the quantitative behavior of the fingers with each other, than to give a qualitative measure for the front interfacial length. The same is true for the growth rate, which takes into account the derivative of the mobility, which is highest behind the front, and thus does not directly reflect the instabilities at the front. However, it is the unstable behavior behind the front that is of interest in this paper. The consequence of this is that the growth rate shows a much higher variation than for the foam case. The average growth rate is more or less constant after an initial increase. The growth rate for the case without foam is decreasing first and later showing a small increase. This could be due to numerical issues, since it wasn't observed by (Riaz and Tchelepi, 2004). The vorticity norm gives a more consistent pattern, which resembles the interfacial length, and after a fast initial growth, shows a slight decrease where after it increases very slowly.

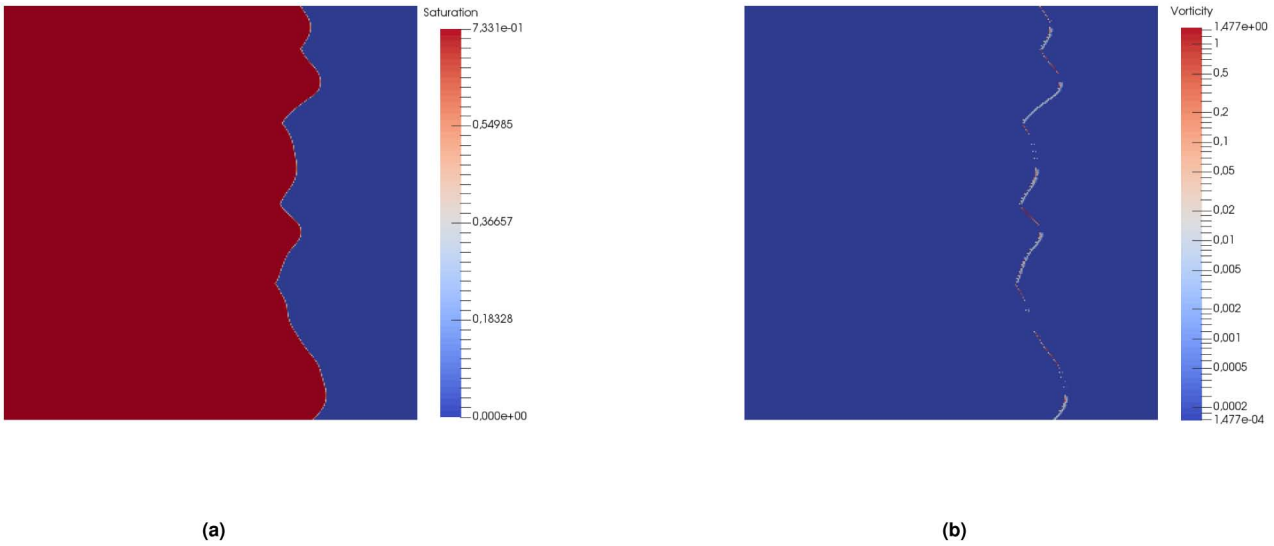

(a) (b)

Figure 12—(a) Saturation profile and (b) vorticity function, for the first test case of Farajzadeh et al. (2016) after 0.53 PV of injected gas.

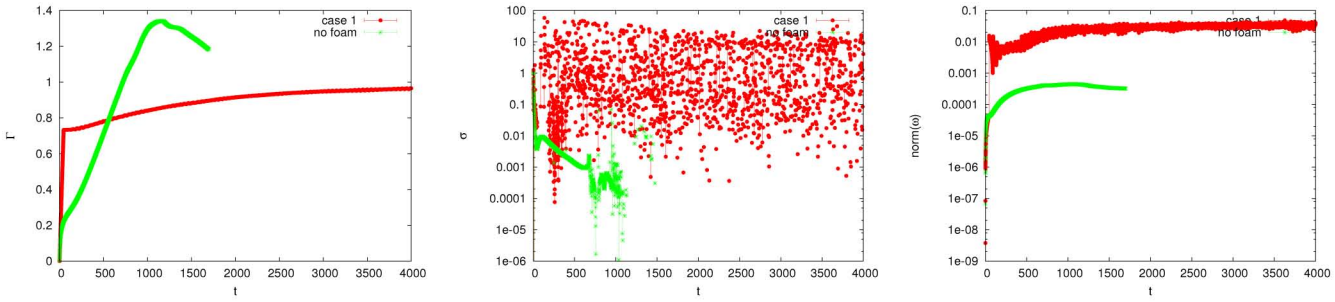

(a) interfacial length (b) growth rate (c) vorticity norm

Figure 13—Numerical approximation of the interfacial length, growth rate and vorticity norm for test case 1 of Farajzadeh et al. (2016).

Test case 2

The second test (Fig. 14) case describes a strong foam, with a high resistance of foam to flow and high critical water saturation, and a very sharp transition from gas to foam (κ). This sharp transition from gas to foam could potentially lead to numerical instability, if not treated with appropriate care (Rossen, 2013), (Van der Meer et al., 2016). It was for this test case that Farajzadeh et al. (2016) observed the viscous pattern behind the front in the apparent viscosity of the foam. For this case we see the same initial increase of the

interfacial length as for the first test case in Fig. 15, after which it keeps constant. The reference case without foam, shows a gradual increase which becomes constant after some time. The growth rate decreases for the model without foam, where after it becomes negative due to the gas reaching the right boundary. For the strong foam model we see again a huge variation in the growth rate, and the vorticity norm shows a steep increase after which it becomes constant. Again, the vorticity norm is higher than for the case without foam, due to the large derivatives of the mobility behind the front.

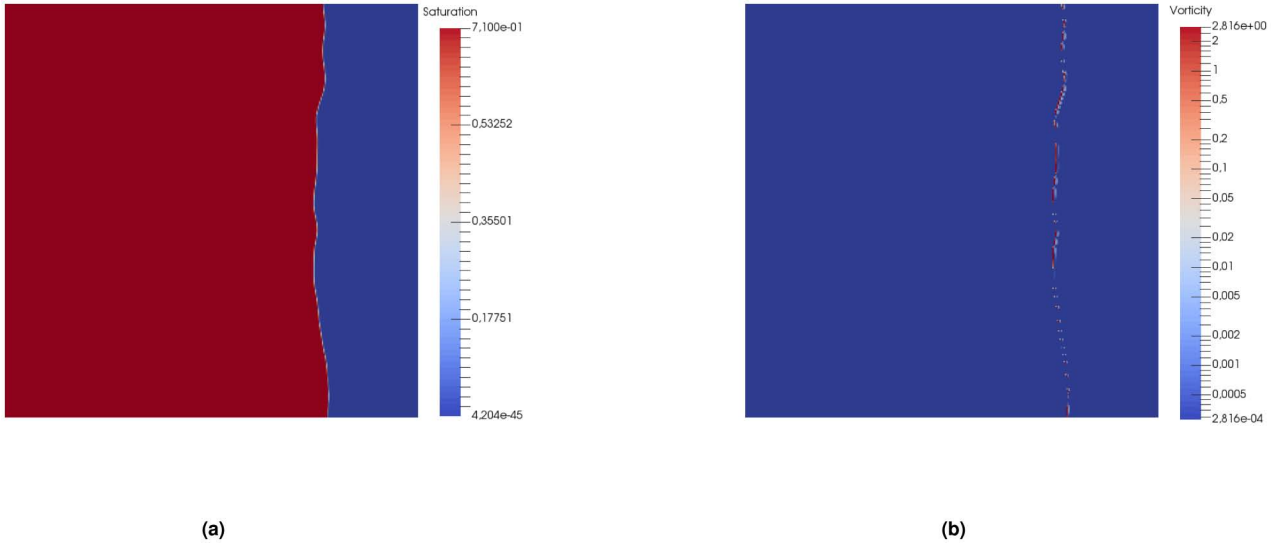

Figure 14—(a) Saturation profile and (b) vorticity function, for the second test case of Farajzadeh et al. (2016) after 0.53 PV of injected gas.

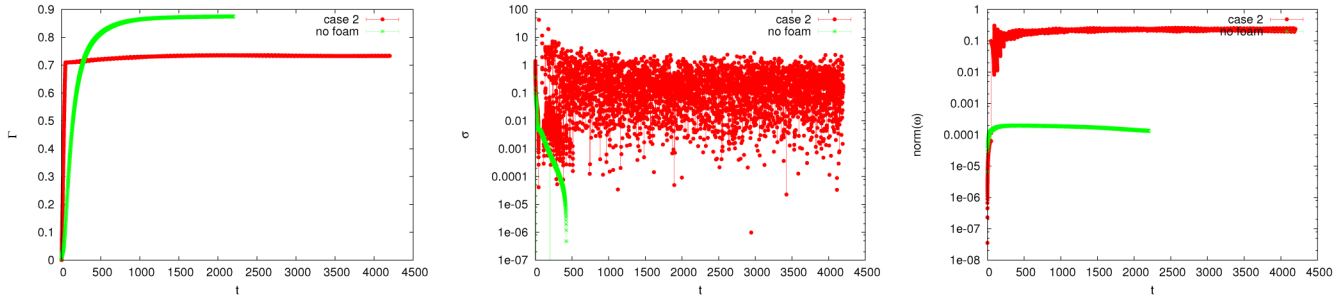

Figure 15—Numerical approximation of the interfacial length, growth rate and vorticity norm for test case 2 of Farajzadeh et al. (2016).

Test case 3

The third test (Fig. 16) case resembles test case 2 and 4, apart from the transition speed from gas to foam, which is a factor 10 lower here than for test case 2 and a factor 10 higher than test case 4. This translates to the stability parameters depicted in Fig. 17, which give almost identical results as for the second test case, but an order 10 smaller for the growth rate and the vorticity norm.

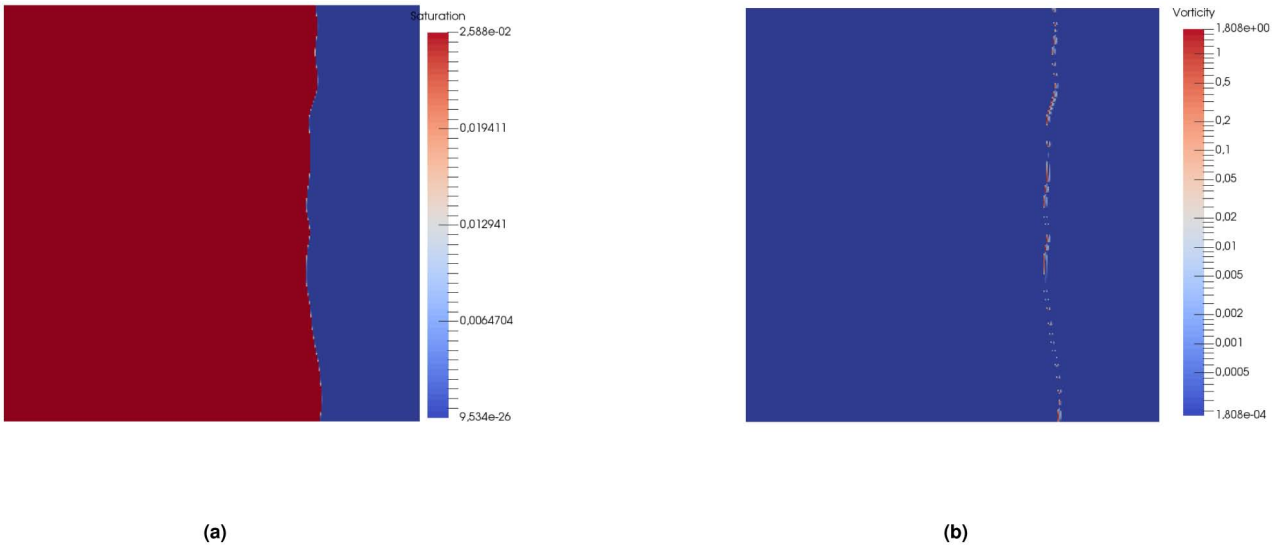

(a) (b)

Figure 16—(a) Saturation profile and (b) vorticity function, for the third test case of Farajzadeh et al. (2016) after 0.53 PV of injected gas.

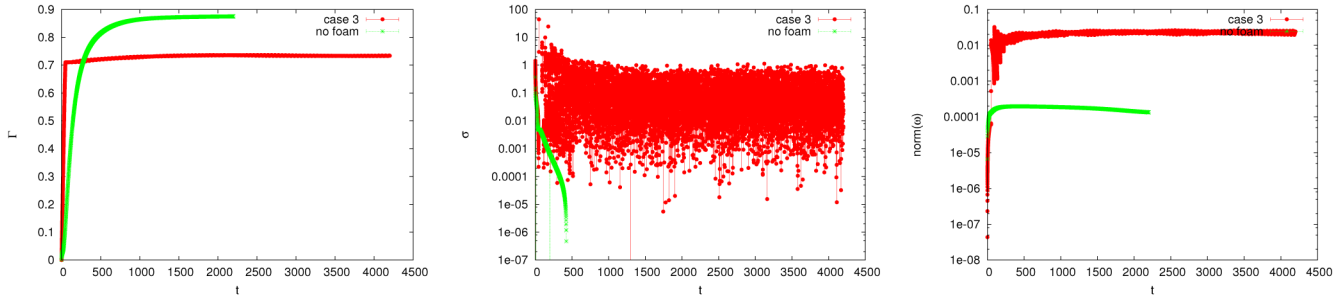

(a) interfacial length (b) growth rate (c) vorticity norm

Figure 17—Numerical approximation of the interfacial length, growth rate and vorticity norm for test case 3 of Farajzadeh et al. (2016).

Test case 4

Test case 4 simulates a strong foam, with a relatively wide transition zone between gas and foam. This means that the numerical method will have no strong stability issues, and the restriction on the time step is less than for the three preceding cases. As shown in Fig. 18 the foam front is stable, since the foam is strong and no fingering behind the front is observed, which is in agreement with the results of Farajzadeh et al. (2016). In Fig. 21 the stability parameters are again very similar to test case 2 and 3, but the growth rate is reduced by an order 1000 with respect to test case 2. Hence, we can assume that for a strong foam (test case 2, 3 and 4) the vorticity norm depends linearly on the parameter κ, i.e.

$$\bar{\omega} \sim \kappa. \tag{31}$$

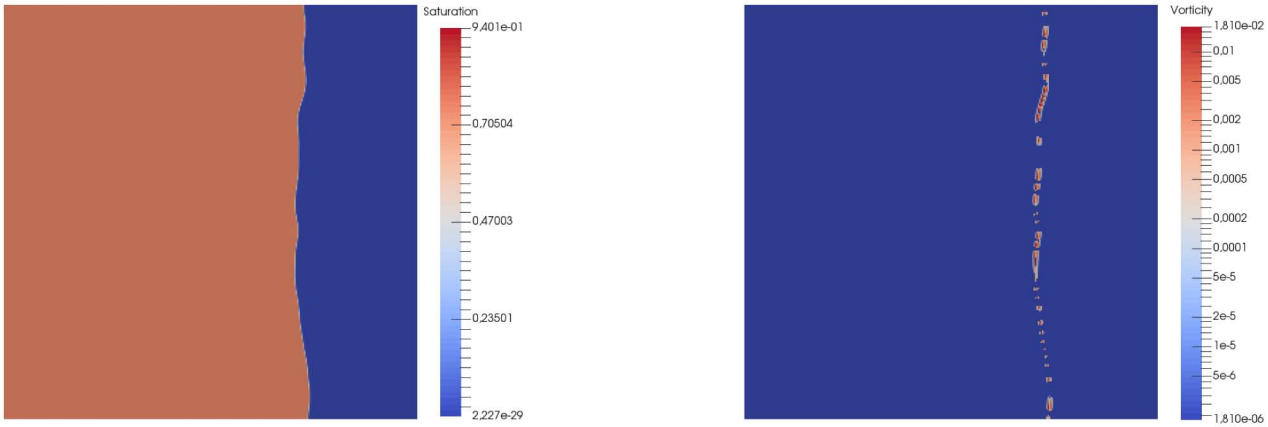

(a) (b)

Figure 18—(a) Saturation profile and (b) vorticity function, for the fourth test case of Farajzadeh et al. (2016) after 0.53 PV of injected gas.

This means that reducing κ by approximately a factor 10, leads to a reduction in the vorticity norm by a factor 10.

Reference case without foam

As a reference, we repeat the above simulations without foam, for test case 1 and 2 in Fig. 19 and 20 (case 3 and 4 only differ in foam transition width to case 2). Since there is no foam present the apparent foam viscosity is equal to the gas viscosity, which is constant everywhere. The difference in the solutions with foam is striking, since the fingers for these two cases are way more pronounced. However, these instabilities seem to be mainly located at the front, while behind the front the saturation front is very smooth.

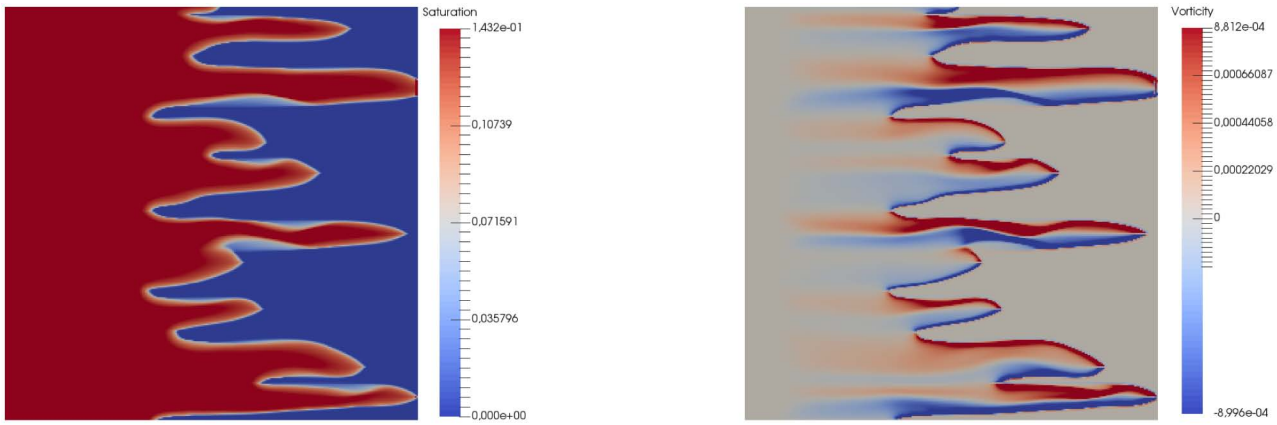

(a) (b)

Figure 19—(a) Saturation profile and (b) vorticity function, for simulation case 1 without foam after 0.53 PV of injected gas.

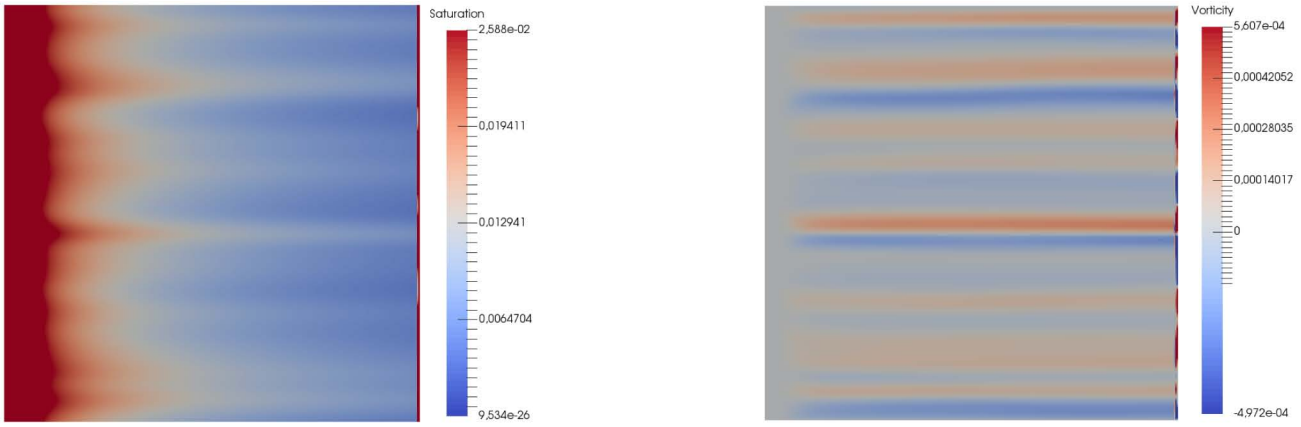

(a) (b)

Figure 20—(a) Saturation profile and (b) vorticity function, for simulation case 2 without foam after 0.22 PV of injected gas.

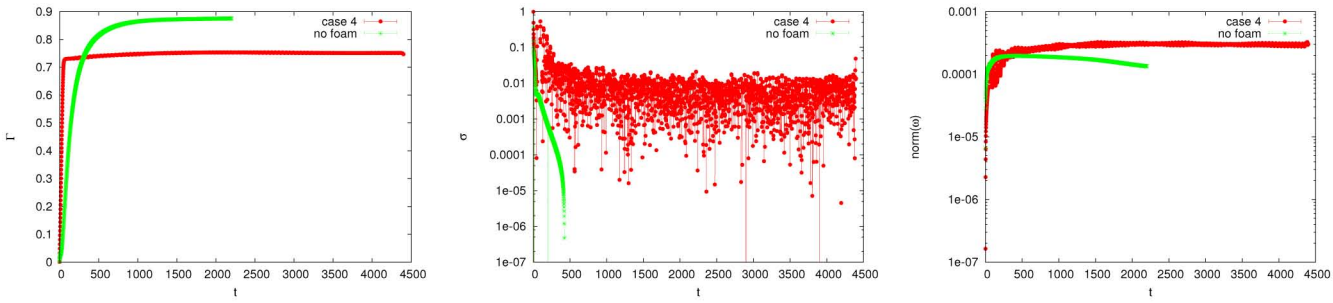

(a) interfacial length (b) growth rate (c) vorticity norm

Figure 21—Numerical approximation of the interfacial length, growth rate and vorticity norm for test case 4 of Farajzadeh et al. (2016).

Discussion

The strong correlation between $\bar{\omega}$ and κ can also be seen in Fig. 22, where the test cases are compared to each other. However, it shows that the vorticity of test case 1 is an order 10 lower than test case 2, although they have the same transition width. This can be due to a lower mobility reduction factor for test case 1 (see Table 1), which causes a smaller mobility derivative around the critical water saturation. Hence a lower vorticity is expected behind the front, whereas an increase in fingering at the front should partly compensate for this. The interfacial length is largest for the cases without foam (until the front second case reaches the right side of domain, and the interfacial length drops below that of the first foam case). After that, the weak foam shows the highest interfacial length, as we could also observe from the saturation plots. The strong foam cases are all really stable at the front and therefore the interfacial length is more or less constant around the same value. On the other hand, the average growth rate of test case 2 is almost as large as for test case 1, which implies that instabilities behind the front must contribute to this result. The average growth rate of the other two test cases are smaller and almost zero. The growth rate for the reference case without foam is not comparable here because of the chosen measure, as explained before.

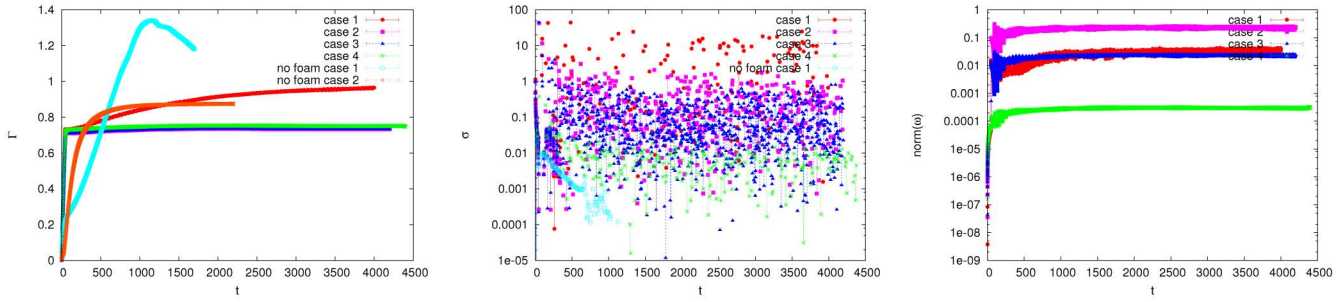

(a) interfacial length (b) growth rate (c) vorticity norm

Figure 22—Numerical approximation of the interfacial length, growth rate and vorticity norm for the first four test cases of Farajzadeh et al. (2016).

If we compare the results with the linear stability analysis, we see that indeed a higher non-linearity (i.e. smaller transition width from gas to foam) leads to more instability behind the front, while the front stays more or less stable as follows from the interfacial length. The influence of the limiting water saturation is not directly clear from the numerical simulations, and more test cases with a wider range of limiting water saturations and mobility reduction factors are needed to investigate this. For example a test case that describes a weak foam with a high transition width, is needed to illustrate the interaction between the different foam parameters and the stability of the numerical results.

Conclusions

The physical instabilities that were observed behind the front in Farajzadeh et al. (2016) seem to be inherent to the nonlinearity in the mobility of foam. We found that a strong foam with a narrow transition width between gas and foam (test case 2) shows the highest growth rate of all test cases, although the front is most stable. We investigated the influence of the parameters that determine foam strength, transition width and critical water saturation on the stability characteristics of the solutions. It shows that a high mobility reduction factor (foam strength) has a stabilizing effect on the solutions, while a higher non-linearity of the gas-foam transition (shorter transition width) has a destabilizing effect. It turns out that the growth rate of instabilities is linearly dependent on both the inverse foam strength and transition width control parameters ($1/R$ and κ). There is also a strong effect of the critical water saturation on the stability characteristics.

In this research we neglected the influence of capillarity in both the linear stability analysis and the simulations, because it has a damping effect on the instabilities at the front. For a more realistic outcome, the affect of additional diffusion can be investigated. Furthermore we could extend this analysis to a quarter-five spot setup. This adds an extra complexity to the model due to a spatially varying strain field that affects the stability front, as was shown for a miscible flow case in Chen and Meiburg (1998). Moreover, we recommend to extend the current local equilibrium foam models to more complex models at the front, to gain more insight in the nature of instabilities that occur behind the foam front and to investigate whether they are able to cause an unstable displacement. In this case models that take into account the gas-foam interface might give an outcome.

Finally the results from the stability analysis can be used to identify important scales and wave lengths of the problem, which in turn can be adapted in building an efficient numerical solver that is able to capture both the fast waves that occur due to the foam, and the slow waves occurring in the rarefaction wave.

Acknowledgements

This research was carried out within the context of the Recovery Factory project at Delft University of Technology (TU Delft), sponsored by Shell Global Solutions International. We would like to thank Dr. Hajibeygi of TU Delft for useful discussions and suggestions about the stability analysis of the foam model.

Also, we would like to thank prof. Rossen of TU Delft for his detailed comments on the draft version of this paper and useful discussions about the physics of foam.

References

Ambrosi, D. and L. Quartapelle (1998). A Taylor–Galerkin Method for Simulating Nonlinear Dispersive Water Waves. *Journal of Computational Physics* **146**(2), 546–569. DOI: 10.1006/jcph.1998.6027.

Ashoori, E., D. Marchesin, and W. R. Rossen (2011). Roles of transient and local equilibrium foam behavior in porous media: Traveling wave. *Colloids and Surfaces A: Physicochemical and Engineering Aspects* **377**(1-3), 228–242.

Ashoori, E., D. Marchesin, and W. R.Rossen (2012). Stability Analysis of Uniform Equilibrium Foam States for EOR Processes. *Transport in Porous Media* **92**(3), 573–595.

Boeije, C. S. and W. R. Rossen (2013, jul). Fitting Foam Simulation Model Parameters for SAG Foam Applications. *In SPE Enhanced Oil Recovery Conference*. Society of Petroleum Engineers. DOI: 10.2118/166244-PA.

Boeije, C. S. and W. R. Rossen (2015, feb). Gas-Injection Rate Needed for SAG Foam Processes To Overcome Gravity Override. *SPE Journal* **20**(01), 049–059. DOI: 10.2118/166244-PA.

Chen, C.-Y. Y. and E. E. Meiburg (1998, sep). Miscible porous media displacements in the quarter five-spot configuration. Part 2. Effect of heterogeneities. *Journal of Fluid Mechanics* **371**(1998), 269–299. DOI: 10.1017/S0022112098002201.

Dahlquist, G. G. (1963). A special stability problem for linear multistep methods. *BIT Numerical Mathematics* **3** (1), 27–43.

Falgout, R. D. and U. Meier Yang (2002). Hypre: a Library of High Performance Preconditioners. *In Preconditioners, Lecture Notes in Computer Science*, pp. 632–641.

Farajzadeh, R., A. A. Eftekhari, H. Hajibeygi, S. Kahrobaei, J. M. van der Meer, S. Vincent-Bonnieu, and W. R. Rossen (2016, aug). Simulation of instabilities and fingering in surfactant alternating gas (SAG) foam enhanced oil recovery. *Journal of Natural Gas Science and Engineering* **34**, 1191–1204. DOI: 10.1016/j.jngse.2016.08.008.

Farajzadeh, R., M. Lotfollahi, A. Eftekhari, W. R. Rossen, and G. J. H. Hirasaki (2015, may). Effect of Permeability on Implicit-Texture Foam Model Parameters and the Limiting Capillary Pressure. *Energy & Fuels* **29**(5), 3011–3018. DOI: 10.1021/acs.energyfuels.5b00248.

Hvistendahl Karlsen, K., K. A. Lie, J. Natvig, H. Nordhaug, and H. Dahle (2001, nov). Operator Splitting Methods for Systems of Convection-Diffusion Equations: Nonlinear Error Mechanisms and Correction Strategies. *Journal of Computational Physics* **173**(2), 636–663. DOI: 10.1006/jcph.2001.6901.

Khatib, Z., G. Hirasaki, and A. Falls (1988, aug). Effects of Capillary Pressure on Coalescence and Phase Mobilities in Foams Flowing Through Porous Media. *SPE Reservoir Engineering* **3**(03), 919–926. DOI: 10.2118/15442-PA.

LeVeque, R. J. (1992). *Numerical Methods for Conservation Laws* (second ed.). Birkhauser Verlag.

Meulenbroek, B., R. Farajzadeh, and H. Bruining (2013). The effect of interface movement and viscosity variation on the stability of a diffusive interface between aqueous and gaseous CO2. *Physics of Fluids* **25**(7), 074103. DOI: 10.1063/1.4813072.

Namdar Zanganeh, M., J. B. F. M. Kraaijevanger, H. W. Buurman, J. D. Jansen, W. R. Rossen, and M. N. Zanganeh (2014, may). Challenges in adjoint-based optimization of a foam EOR process. *Computational Geosciences* **18**(3-4), 563–577.

Riaz, A., M. Hesse, H. A. Tchelepi, and F. M. Orr (2005, feb). Onset of convection in a gravitationally unstable diffusive boundary layer in porous media. *Journal of Fluid Mechanics* **548**(-1), 87–111. DOI: 10.1017/S0022112005007494.

Riaz, A. and H. A. Tchelepi (2004, nov). Linear stability analysis of immiscible two-phase flow in porous media with capillary dispersion and density variation. *Physics of Fluids* **16**(12), 4727–4737. DOI: 10.1063/1.1812511.

Riaz, A. and H. A. Tchelepi (2006a, sep). Influence of Relative Permeability on the Stability Characteristics of Immiscible Flow in Porous Media. *Transport in Porous Media* **64**(3), 315–338.

Riaz, A. and H. A. Tchelepi (2006b, jan). Numerical simulation of immiscible two-phase flow in porous media. *Physics of Fluids* **18**(1), 014104. DOI: 10.1063/1.2166388.

Riaz, A. and H. A. Tchelepi (2007). Stability of two-phase vertical flow in homogeneous porous media. *Physics of Fluids* **19**(7), 072103. DOI: 10.1063/1.2742975.

Rossen, W. R. (2013). SPE 16624432 Numerical Challenges in Foam Simulation : A Review. In SPE Annual Technical Conference and Exhibition held in New Orleans, Number October, New Orleans. SPE International.

Toro, E. F. (2009). *Riemann Solvers and Numerical Methods for Fluid Dynamics* (third ed.). Springer Berlin / Heidelberg.

Van der Meer, J. M., J. B. F. M. Kraaijevanger, M. Möller, and J. D. Jansen (2016). Temporal oscillations in the simulation of foam enhanced oil recovery. In Proc. 15th European Conference on Mathematics in Oil Recovery (ECMOR XIV), Amsterdam. DOI: 10.3997/2214-4609.201601850.

Van der Meer, J. M., D. E. A. Van Odyck, P. Wirnsberger, and J. D. Jansen (2014, sep). High-order Simulation of Foam Enhanced Oil Recovery. In Proc. 14th European Conference on Mathematics in Oil Recovery (ECMOR XIV), Catania, pp. 8–11.

Wirnsberger, P. (2012). *The grid orientation effect in miscible displacement*. Mphil dissertation, University of Cambridge.

Yahya Afiff, I. (2014). *Reservoir simulation of foam flow using Kepler GPU*. Msc. thesis, Delft University of Technology.

Yortsos, Y. and F. J. Hickernell (1989). Linear Stability of Immiscible Displacement Processes in Porous Media. *SIAM J. Appl.\ Math*. **49**(3), 730–748.

Appendix A:
Derivation two-phase flow equations

In the following sections we give a derivation of the non-dimensional incompressible, immiscible two-phase flow equations for gas and water and foam in a porous medium. Mass conservation of each phase, is described by a mass-balance equation for the phase saturation $S_\alpha \in [0, 1]$, given by

$$\phi \partial_t S_\alpha = -\nabla \cdot \mathbf{u}_\alpha, \tag{32}$$

where the subscript $\alpha \in \{w,g,f\}$ denotes the phase (water, gas or foam in this case), ϕ denotes the reservoir porosity, and $\mathbf{u}_\alpha$ the phase velocity that is given by

$$\mathbf{u}_\alpha = -\lambda_\alpha (\nabla P_\alpha + \rho_\alpha \mathbf{g}). \tag{33}$$

Here P_α is the phase pressure, ρ_α is the phase density, $\mathbf{g}$ is the gravitational force, and λ_α is the phase mobility

$$\lambda_\alpha = k \frac{k_{r\alpha}(S_\alpha)}{\mu_\alpha}, \tag{34}$$

where k is the absolute permeability, μ_α the phase viscosity and $k_{r\alpha}$ the phase relative permeability, which is defined in the main part of this article.

Two-phase flow In case of two fluids, the difference between the phase pressures is described by the capillary pressure, defined as

$$P_c \equiv P_w - P_g, \tag{35}$$

such that

$$\mathbf{u}_w = -\lambda_w (\nabla P_c + \nabla P_g + \rho_w \mathbf{g}), \tag{36}$$

$$\mathbf{u}_g = -\lambda_g (\nabla P_g + \rho_g \mathbf{g}). \tag{37}$$

The total velocity, which is the sum of the phase velocities, is thus equal to

$$\mathbf{u} = -[\lambda_T \nabla P_g + \lambda_w \nabla P_c + (\lambda_w \rho_w + \lambda_g \rho_g)\mathbf{g}], \tag{38}$$

where λ_T is the total mobility (sum of mobilities). Hence, we can express the phase velocity of water in terms of the total velocity as follows

$$\mathbf{u}_w = -\lambda_w \nabla P_c + \frac{\lambda_w}{\lambda_T}(\mathbf{u} + \lambda_w \nabla P_c + \lambda_g(\rho_g - \rho_w)\mathbf{g}) \tag{39}$$

$$= \frac{\lambda_w}{\lambda_T}\mathbf{u} - \frac{\lambda_w \lambda_g}{\lambda_T}(\nabla P_c + \Delta\rho \mathbf{g}) \tag{40}$$

$$= f_w \mathbf{u} - \lambda_w f_g (\nabla P_c + \Delta\rho \mathbf{g}), \tag{41}$$

where $f_\alpha = \lambda_\alpha/\lambda_T$ is the phase fractional flow function and $\Delta\rho = \rho_w - \rho_g$. Hence we can express Eq. 32 as

$$\phi \partial_t S_w = -\nabla \cdot (f_w (\mathbf{u} - \lambda_g (P_c' \nabla S_w + \Delta\rho \mathbf{g}))), \tag{42}$$

where P_c' is the derivative of the capillary pressure with respect to the phase saturation, that is approximated by (Riaz and Tchelepi, 2004)

$$P_c' = \sqrt{\frac{\phi}{k}} \gamma_{gw} \sin(\theta). \tag{43}$$

where γ_{gw} is the interfacial tension between gas and water and θ the tilting angle of the rectangular domain with respect to the gravitational force. From the definition of saturation it follows that the sum of the phase saturations is one everywhere, i.e.

$$\sum_{\alpha} S_{\alpha} = 1, \text{ with } \alpha \in \{w, g\}, \tag{44}$$

so that we only have to solve for one phase. Hence, Eq. 41, 42 and 44 imply that

$$\nabla \mathbf{u} = 0. \tag{45}$$

which describes the pressure decay in the porous medium.

Non-dimensional formulation

To reduce the number of parameters we scale the model given by Eq. 32, 33 and 45, in a similar way as done by (Riaz and Tchelepi, 2004). If we let U be a characteristic velocity scale, L a characteristic length scale of the model, and W a characteristic width scale, such that $A = L/W$ is the aspect ratio, we can scale the other variables as follows

$$x = L\tilde{x}, \tag{46}$$

$$y = W\tilde{y}, \tag{47}$$

$$\nabla = \frac{\tilde{\nabla}}{L}, \tag{48}$$

$$\mathbf{u} = U\tilde{\mathbf{u}}, \tag{49}$$

$$t = \frac{\phi L(1 - S_{wc} - S_{gr})}{U}\tilde{t}, \tag{50}$$

$$P = \frac{\mu U L}{k}\tilde{P}, \tag{51}$$

$$P'_c = \gamma_{gw}\sqrt{\frac{\phi}{k}}\tilde{P}'_c, \tag{52}$$

where the tilde denotes a non-dimensional variable. The relative permeability functions are scaled by their endpoint relative permeabilities, i.e. the relative permeability of the residual water and gas saturation, $k_{rwe} = k_{rw}(S_{gr})$ and $k_{rge} = k_{rg}(1 - S_{wc})$, respectively. The gas saturation is normalized by $\tilde{S}_g = \frac{(S_g - S_{gr})}{(1 - S_{wc} - S_{gr})}$. Substituting these variables into the two-dimensional model leads to a non-dimensional system of the form

$$\partial_{\tilde{t}}\tilde{S}_g = -\tilde{\nabla}\cdot\left[M\frac{\tilde{k}_{rg}}{\tilde{\lambda}}\left(\tilde{\mathbf{u}} - \frac{\tilde{k}_{rw}}{N_{ca}}\tilde{P}'_c\tilde{\nabla}\tilde{S}_g - \tilde{k}_{rw}\frac{G}{M}\tilde{\nabla}z\right)\right], \tag{53}$$

$$\tilde{\mathbf{u}} = -\tilde{\lambda}_w\tilde{\nabla}\tilde{P}_c - \tilde{\lambda}\tilde{\nabla}\tilde{P}_g - \lambda_w G\nabla z, \tag{54}$$

$$\tilde{\nabla}\tilde{\mathbf{u}} = 0, \tag{55}$$

where $\tilde{\lambda} = M\tilde{k}_{rg} + \tilde{k}_{rw}$ is the dimensionless mobility function. Here, the variables M, G and N_c denote the end-point mobility ratio, gravity number and capillary number respectively, which are given by

$$M = \frac{\mu_w}{\mu_g}\frac{k_{rge}}{k_{rwe}}, \tag{56}$$

$$G = \frac{k\Delta\rho g}{\mu_g U}, \tag{57}$$

$$N_{ca} = \frac{U\mu_w}{\gamma_{gw}\sin(\theta)}, \tag{58}$$

where g is the magnitude of the gravitational force. The mobility ratio together with the dimensionless foam parameters R, κ and S_w*, the dimensionless injection rate $\tilde{f}$ and the porosity ϕ, determine the entire behavior of the fluids for a certain initial boundary value problem.

In the rest of the article we will drop the tilde for readability and define $S \equiv S_g$ and $f \equiv \frac{k_{rg}M}{\tilde{\lambda}}$.

Appendix B:
Derivation perturbation equations

Here we derive the equations used for the stability analaysis, that is described in (Riaz and Tchelepi, 2007). For this we rewrite Eq. 53 and 55 in terms of the transformed variable $\xi = x - v_s t$, y and t, so that

$$\partial_t S - v_s \partial_\xi S + \nabla \cdot (k_{rw} \nabla \bar{P}) = 0, \tag{59}$$

$$\nabla \cdot \left(\lambda \nabla \bar{P} - G k_{rg} \nabla z - \frac{k_{rg}}{\mathrm{Ca}} P_c' \nabla S \right) = 0 \tag{60}$$

Substitute $(S, P)(\xi,y,t)=(S_0,P_0)(\xi)+(\hat{s}, \hat{p})\,(\xi)e^{iny + \sigma t}$ in Eq. 59 gives

$$\begin{aligned} &\partial_t S - v_s \partial_\xi S + \partial_x i(k_{rw} \partial_x i \bar{P}) + \partial_y (k_{rw} \partial_y \bar{P}) = 0 \\ \Rightarrow\ &\partial_t S + \partial_\xi \left(k_{rw} \partial_\xi \bar{P} - v_s S \right) + k_{rw} \partial_{yy} \bar{P} + k_{rw}' \partial_y S \partial_y \bar{P} = 0. \end{aligned} \tag{61}$$

Evaluating all derivatives to y and t leads to

$$\sigma \hat{s} e^{iny+\sigma t} + \partial_\xi \left(k_{rw} \left(P_0' + \hat{p}' e^{iny+\sigma t} \right) - v_s \left(S_0 + \hat{s} e^{iny+\sigma t} \right) \right) = n^2 k_{rw} \hat{p} e^{iny+\sigma t} + n^2 k_{rw}' \hat{s} \hat{p} (e^{iny+\sigma t})^2. \tag{62}$$

Multiplying the equation with $e^{-(iny + \sigma t)}$gives

$$\sigma \hat{s} + \partial_\xi \left(k_{rw} P_0' e^{-(iny+\sigma t)} + k_{rw} \hat{p}' - v_s S_0 e^{-(iny+\sigma t)} - v_s \hat{s} \right) = n^2 k_{rw} \hat{p} + n^2 k_{rw}' \hat{s} \hat{p} e^{iny+\sigma t}. \tag{63}$$

Now, we express $k_{rw}(S)$ in terms of S_0 by using a Taylor expansion, such that

$$k_{rw}(S) = k_{rw}(S_0) + k_{rw}'(S_0)(S - S_0) + O((\Delta S)^2) = k_{rw}(S_0) + k_{rw}'(S_0) \hat{s} \exp(inx + \sigma t) + O((\hat{s})^2)). \tag{64}$$

Substituting this in the above equation we obtain

$$\begin{aligned} \sigma \hat{s} + \partial_\xi \Big(&k_{rw} P_0' e^{-(iny+\sigma t)} + k_{rw}' P_0' \hat{s} + k_{rw} \hat{p}' + k_{rw}' \hat{p} \hat{s}' e^{iny+\sigma t} - v_s S_0 e^{-(iny+\sigma t)} - v_s \hat{s} \Big) \\ &= n^2 k_{rw} \hat{p} + n^2 k_{rw}' \hat{s} \hat{p} e^{iny+\sigma t} + n^2 k_{rw}'' \hat{s}^2 \hat{p} e^{2 \cdot (inx+\sigma t)} + O((\hat{s})^2)). \end{aligned} \tag{65}$$

Neglecting all the higher order terms that include $\hat{s}\hat{p}$, $\hat{s}^2$ and $\hat{s}\hat{p}'$, and assuming that $e^{-(iny+\sigma t)} \to 0$ if $\sigma > 0$ for large t, we find that

$$\sigma \hat{s} + \partial_\xi \left(k_{rw}(S_0) \hat{p}' + \left(k_{rw}(S_0)' P_0' - v_s \right) \hat{s} \right) = n^2 k_{rw}(S_0) \hat{p}. \tag{66}$$

We apply the same technique to Eq. 60, such that

$$\begin{aligned} &\partial_\xi \left(\lambda \partial_\xi \bar{P} - G k_{rg} - \frac{k_{rg}}{\mathrm{Ca}} P_c' \partial_\xi S \right) = -\partial_y \left(\lambda \partial_y \bar{P} - \frac{k_{rg}}{\mathrm{Ca}} P_c' \partial_y S \right) \\ \Rightarrow\ &\partial_\xi \left(\lambda (P_0' + \hat{p}' e^{iny+\sigma t}) - G k_{rg} - \frac{k_{rg}}{\mathrm{Ca}} P_c' (S_0' + \hat{s}' e^{iny+\sigma t}) \right) = n^2 \lambda \hat{p} e^{iny+\sigma t} - n^2 \frac{k_{rg}}{\mathrm{Ca}} P_c' \hat{s} e^{iny+\sigma t} \\ \Rightarrow\ &\partial_\xi \left(\lambda (P_0' e^{-(iny+\sigma t)} + \hat{p}') - G k_{rg} e^{-(iny+\sigma t)} - \frac{k_{rg}}{\mathrm{Ca}} P_c' (S_0' e^{-(iny+\sigma t)} + \hat{s}') \right) = n^2 \lambda \hat{p} - n^2 \frac{k_{rg}}{\mathrm{Ca}} P_c' \hat{s}. \end{aligned} \tag{67}$$

We can express $\lambda(S)$, $k_{rg}(S)$ and $P_c'(S)$ in terms of S_0 with a second order accurate Taylor expansion. Neglecting higher order terms, that contain multiples of $\hat{s}$ and $\hat{p}$ or $\hat{p}'$, and letting $e^{-(iny+\sigma t)} \to 0$ leads to

$$\partial_\xi \left(\lambda \hat{p}' + \left(\lambda' P_0' - G k_{rg}' - \frac{1}{\mathrm{Ca}} (k_{rg} P_c')' S_0' \right) \hat{s} - \frac{k_{rg}}{\mathrm{Ca}} P_c' \hat{s}' \right) = n^2 \lambda \hat{p} - n^2 \frac{k_{rg}}{\mathrm{Ca}} P_c' \hat{s}. \tag{68}$$

Eq. 66 and 68 described an eigenvalue problem with eigenvalue σ, in terms of the eigenfunctions $\hat{s}$ and $\hat{p}$:

$$\sigma\hat{s}+\partial_\xi\left(k_{rw}\hat{p}'+\left(k'_{rw}P'_0-v_s\right)\hat{s}\right) = n^2k_{rw}\hat{p}, \tag{69}$$

$$\partial_\xi\left(\lambda\hat{p}'+\left(\lambda'P'_0-Gk'_{rg}-\frac{1}{\mathrm{Ca}}(k_{rg}P'_c)'S'_0\right)\hat{s}-\frac{k_{rg}}{\mathrm{Ca}}P'_c\hat{s}'\right) = n^2\lambda\hat{p}-n^2\frac{k_{rg}}{\mathrm{Ca}}P'_c\hat{s}, \tag{70}$$

where the functions k_{rw},k_{rg} and P_c are functions of S_0, and the apostroph denotes the derivative with respect to S_0 or ξ respectively. The base state functions S_0 and P_0 obey the boundary values of the Buckley-Leverett problem and obtain their maximum gradient at $\xi = 0$, and the eigenfunctions $(\hat{s},\hat{p}) = 0$ and $(\hat{s}',\hat{p}') = 0$ at $\xi = \pm\infty$. This system can be solved numerically (Riaz and Tchelepi, 2004), or by matched asymptotic expansions (Riaz and Tchelepi, 2007).

In the absence of capillarity ($\mathrm{Ca} \to \infty$) the base state satisfies

$$\frac{S_0}{d\xi} = \delta(\xi), \tag{71}$$

$$\frac{dP_0}{d\xi} = \frac{Gk_{rg}-1}{\lambda}, \tag{72}$$

so that it follows from the interface and boundary conditions, that $\hat{s} = c_1\delta(\xi)$, $\forall\xi \in (-\infty, \infty)$ and $c_1 \in \mathbb{R}$ (Riaz and Tchelepi, 2007). Away from the discontinuity at $\xi = 0$, Eq. 69 implies that

$$\partial_\xi\left(k_{rw}\hat{p}'\right) = n^2k_{rw}\hat{p} \quad\Rightarrow\quad \hat{p}'' = n^2\hat{p} \quad\Rightarrow\quad \hat{p} = ce^{\pm n\xi}. \tag{73}$$

Since $\hat{p} = \hat{p}' = 0$ at $\xi = \pm\infty$ it follows that

$$\hat{p}^{+0} = c_2\mathrm{e}^{-n\xi}, \quad \forall\xi > 0, c_2 \in \mathbb{R}, \tag{74}$$

$$\hat{p}^{-0} = c_3\mathrm{e}^{+n\xi}, \quad \forall\xi < 0, c_2 \in \mathbb{R}. \tag{75}$$

Integrating the full system with capillarity given by Eq. 69 and 70 over the discontinuity (from 0^{-0} to 0^{+0}), gives us two equations in terms of p^{+0}, p^{-0} and σ:

$$k_{rw}(S_0(0^{+0}))\hat{p}'^{+0} - k_{rw}(S_0(0^{-0}))\hat{p}'^{-0} = -c_1\sigma, \tag{76}$$

$$\lambda(S_0(0^{+0}))\hat{p}'^{+0} - \lambda(S_0(0^{-0}))\hat{p}'^{-0} = 0. \tag{77}$$

Evaluating the indefinite integral of Eq. 69 over ξ leads to

$$\hat{p}' + c_1(\lambda'P_0 - Gk_{rg})\delta(\xi) = c_4/\lambda + n^2\int\hat{p}d\xi. \tag{78}$$

Rewriting the the terms between brackets as $-P''_0/\delta(\xi)$ by differentiating Eq. 72 with respect to ξ, gives

$$\hat{p}' - c_1P''_0 = c_4/\lambda + n^2\int\hat{p}d\xi. \tag{79}$$

Integrating this expression over the discontinuity gives a third equation in terms of $\hat{p}^{+0}$ and $\hat{p}^{-0}$:

$$\hat{p}^{+0} - \hat{p}^{-0} = c_1(P'^{+0}_0 - P'^{-0}_0). \tag{80}$$

Eq. 76, 77 and 80 then lead to an expression for the disturbance velocity:

$$\frac{\sigma}{n} = \frac{f_{g_1}-f_{g_0}}{S_1-S_0}\frac{\lambda_1(1-Gk_{rg_0})-\lambda_0(1-Gk_{rg_1})}{\lambda_1-\lambda_0}, \tag{81}$$

where the subscripts 0 and 1 denote the front and back edge of the shock respectively.

Appendix C:
Model parameters